

# Novel formulations of microscopic boundary-value problems in continuous multiscale finite element methods

Brian S. Mercer, Kranthi K. Mandadapu, Panayiotis Papadopoulos\*

*Department of Mechanical Engineering, University of California, Berkeley, CA 94720-1740, USA*

Received 20 February 2014; received in revised form 13 October 2014; accepted 15 December 2014

Available online 27 December 2014

## Abstract

This article explores the use of a homogenization method inspired by the classical Irving–Kirkwood procedure in the continuous multiscale modeling of elastic solids within the context of the finite element method. This homogenization method gives rise to a broad range of allowable boundary conditions for the RVE, which, in turn, yield a rich spectrum of estimates of the macroscopic stress response for two representative problems involving heterogeneous elastic bodies.

© 2014 Elsevier B.V. All rights reserved.

**Keywords:** Multiscale; Homogenization; Finite element method; Irving–Kirkwood procedure; Hill–Mandel condition; RVE boundary conditions

## 1. Introduction

Many natural and engineered solids exhibit complex heterogeneous microstructures which may be challenging to characterize using classical macroscopic material constitutive laws. One approach in modeling such materials is to assume that macroscopic variables, such as stress and heat flux, are locally determined via homogenization of the appropriate microscopic variables. When both the macroscopic and the microscopic scale can be accurately analyzed using continuum modeling, computational homogenization may be effected by means of the so-called  $FE^2$  method [1–5]. This explicitly resolves the material microstructure at select macroscopic points (which typically correspond to integration points of the macroscopic finite element mesh) using a finite element-based representative volume element (RVE), thus circumventing the need for full finite element resolution of the entire microstructure in a single scale. In recent years, the  $FE^2$  method has been applied with success to polycrystalline materials [6], materials with voids [7], fiber-reinforced composites [8], and fabrics [9], as well as materials exhibiting coupled thermomechanical response [10] or microstructural phase transition [11].

The Hill–Mandel criterion [12,13] forms the theoretical basis of the vast majority of continuous multiscale modeling implementations to date. This criterion comprises intuitive *a priori* assumptions relating stress, deformation and virtual work across scales. Notwithstanding its widespread use, the Hill–Mandel criterion has several significant limitations. First, boundary conditions imposed on the RVE in the microscale must be consistent with the Hill–Mandel

\* Corresponding author.

E-mail address: [panos@me.berkeley.edu](mailto:panos@me.berkeley.edu) (P. Papadopoulos).

assumptions, resulting in a limited set of allowable such boundary conditions. Since the homogenized material response may depend strongly on the specific choice of RVE boundary conditions [14,15], this limitation may lead to inaccurate approximation of the true homogenized material response, especially when the latter deviates from periodicity (e.g., near exterior boundaries or interior surfaces of discontinuity). Second, the Hill–Mandel assumptions presume a quasi-static microscale relative to the macroscale dynamics based on time-scale separation arguments [11], which precludes the study of microscale inertial effects. Finally, the Hill–Mandel criterion appears to have no direct extension to thermal variables, thus necessitating the introduction of additional assumptions for thermomechanical homogenization problems. As Hill himself observed in connection with the definition of the macroscopic deformation and stress [13]: “It is not necessary, by any means, that macro-variables so defined should be unweighted volume averages of their microscopic counterparts. However, variables that do have this special property are naturally the easiest to handle analytically in the transition between levels”. Indeed, there is no fundamental principle underlying the assumptions of the Hill–Mandel criterion other than analytical ease and conceptual plausibility.

Recently, a general continuum homogenization theory has been proposed [16] which is inspired by the classical Irving–Kirkwood procedure for upscaling atomistic variables to the continuum level [17]. The governing principle of this theory is that only fundamental extensive quantities of continuum thermomechanics (here, mass, momentum, and energy) should be volume-averaged over the microscale. As long as the continuum balance laws apply at both scales, this theory gives rise to expressions for the macroscopic stress and heat flux in terms of the microscopic kinematic and kinetic variables. The general framework of this theory allows the freedom to derive a broad range of RVE boundary conditions that communicate to the microscale sufficient evidence of the local macroscopic deformation, as well as to investigate the role of microscale thermal and inertial effects in the homogenized material response. Within the general theory, this article explores the RVE boundary-value problem and, in particular, the development of novel handshake conditions for the purely mechanical homogenization problem which transcend the Hill–Mandel criterion. Such conditions are formally derived both for finite and infinitesimal deformations and their practical implementation is considered within the context of the finite element method. In addition, it is shown that these conditions yield homogenized responses that differ from those obtained from the imposition of displacement, traction and periodic boundary conditions that are compatible with the Hill–Mandel criterion.

The remainder of this article is organized as follows: Section 2 summarizes the important ideas behind the continuum Irving–Kirkwood theory, and demonstrates its generality compared to the Hill–Mandel criterion. In Section 3, novel RVE boundary-value problems are introduced consistently with the continuum Irving–Kirkwood theory, and their finite element implementation is discussed. Section 4 includes two purely mechanical and quasistatic example problems which illustrate the homogenization properties of the proposed RVE boundary-value problems. This is followed by a reflection on the findings in Section 5.

## 2. Continuum homogenization theory

The theory proposed in [16] based on the classical Irving–Kirkwood procedure offers a rigorous and general approach to continuum homogenization. This theory relies on the following three fundamental assumptions:

1. The material of interest may be approximated as a continuum at the macroscopic and microscopic scales.
2. The conservation laws for mass, momentum, and energy hold at the macroscopic and microscopic scales.
3. Homogenization in the form of weighted averaging is effected on the three principal extensive quantities of continuum mechanics, that is, mass, linear momentum, and energy.

In the remainder of this section, the continuum Irving–Kirkwood theory is summarized and its relation to the Hill–Mandel approach is discussed.

### 2.1. Continuum balance laws

By way of background, the classical balance laws of continuum mechanics for purely mechanical processes are stated here in both spatial and referential form.

Consider a body  $\mathcal{B}$  occupying a region  $\mathcal{R}$  at time  $t$ . The integral forms of balance of mass and linear momentum for any region  $\mathcal{P} \subset \mathcal{R}$  with boundary  $\partial\mathcal{P}$  are

$$\frac{d}{dt} \int_{\mathcal{P}} \rho \, dv = 0 \quad (1)$$

and

$$\frac{d}{dt} \int_{\mathcal{P}} \rho \mathbf{v} dv = \int_{\partial \mathcal{P}} \mathbf{t} da + \int_{\mathcal{P}} \rho \mathbf{b} dv, \quad (2)$$

respectively. Here,  $\rho$  is the mass density,  $\mathbf{v}$  the velocity,  $\mathbf{t}$  the traction on  $\partial \mathcal{P}$ , and  $\mathbf{b}$  the body force per unit mass. The corresponding local forms of these balance laws are

$$\dot{\rho} + \rho \operatorname{div} \mathbf{v} = 0 \quad (3)$$

and

$$\operatorname{div} \mathbf{T} + \rho \mathbf{b} = \rho \dot{\mathbf{v}}. \quad (4)$$

Here,  $\mathbf{T}$  is the Cauchy stress and “div” denotes the spatial divergence operator. Also,  $\dot{(\cdot)}$  is a shorthand notation for the material time derivative of  $(\cdot)$ .

The balance laws may be expressed alternatively with respect to a reference configuration  $\mathcal{R}_0$  occupied by the body  $\mathcal{B}$  at time  $t_0$ . For any region  $\mathcal{P}_0 \subset \mathcal{R}_0$  with boundary  $\partial \mathcal{P}_0$ , the integral statements of the balance of mass and linear momentum are

$$\frac{d}{dt} \int_{\mathcal{P}_0} \rho_0 dV = 0 \quad (5)$$

and

$$\frac{d}{dt} \int_{\mathcal{P}_0} \rho_0 \mathbf{v} dV = \int_{\partial \mathcal{P}_0} \mathbf{p} dA + \int_{\mathcal{P}_0} \rho_0 \mathbf{b} dV, \quad (6)$$

respectively. In this case,  $\rho_0$  is the referential mass density, while  $\mathbf{p}$  is the traction at time  $t$  resolved on  $\partial \mathcal{P}_0$ . The corresponding local forms are

$$\dot{\rho}_0 = 0 \quad (7)$$

and

$$\operatorname{Div} \mathbf{P} + \rho_0 \mathbf{b} = \rho_0 \dot{\mathbf{v}}, \quad (8)$$

where  $\mathbf{P}$  stands for the first Piola–Kirchhoff stress and “Div” for the referential divergence operator.

## 2.2. Continuum Irving–Kirkwood theory

In this section, the most important findings of the continuum Irving–Kirkwood theory are summarized for the purely mechanical case. The reader may refer to [16] for a complete development of the theory.

Assume that for the region  $\mathcal{R}$  occupied by the body there exists a microscopic (fine) scale and a macroscopic (coarse) scale with the latter’s properties being derived from the homogenization of fine scale variables. As such, let a typical macroscopic point be denoted  $\mathbf{y}$ . Associated with each macroscopic point is a microscopic region  $\omega$  with volume  $v$ , and a typical point in  $\omega$  is denoted  $\mathbf{x}$ , as in Fig. 1. In this section, it will be necessary to distinguish between spatial derivatives with respect to  $\mathbf{x}$  and  $\mathbf{y}$  coordinates; hence, the notation  $\frac{\partial}{\partial \mathbf{x}} \cdot (\cdot)$  and  $\frac{\partial}{\partial \mathbf{y}} \cdot (\cdot)$  (resp.  $\frac{\partial}{\partial \mathbf{x}} (\cdot)$  and  $\frac{\partial}{\partial \mathbf{y}} (\cdot)$ ) will be used to denote the divergence (resp. gradient) operator in each coordinate system. An analogous notation will be employed when divergences or gradients are taken with respect to referential coordinates  $\mathbf{X}$  and  $\mathbf{Y}$ .

The essential link between the two scales is provided by the homogenization of mass and linear momentum, in the form

$$\rho^M(\mathbf{y}, t) = \int_{\mathcal{R}} \rho^m(\mathbf{x}, t) g(\mathbf{y}, \mathbf{x}) dv^m \quad (9)$$

and

$$\rho^M(\mathbf{y}, t) \mathbf{v}^M(\mathbf{y}, t) = \int_{\mathcal{R}} \rho^m(\mathbf{x}, t) \mathbf{v}^m(\mathbf{x}, t) g(\mathbf{y}, \mathbf{x}) dv^m. \quad (10)$$

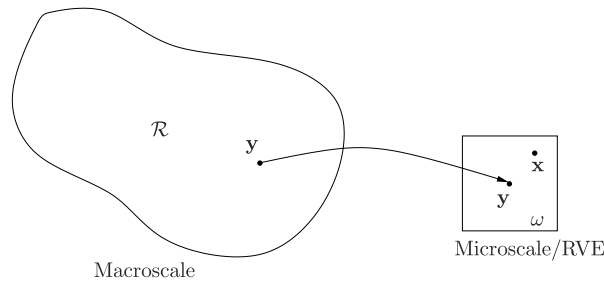


Fig. 1. Schematic of the representation of the two scales, with positions in each denoted by the vectors  $\mathbf{y}$  and  $\mathbf{x}$ .

Eqs. (9)–(10) express the assumption that the macroscopic mass and linear momentum densities at a macroscopic material point are computed as weighted averages of the same quantities in a microstructural region associated with that point. Note that macroscopic quantities in (9)–(10) and henceforth are signified by superscript  $M$  and are functions of  $\mathbf{y}$  and  $t$ , while microscopic quantities are signified by superscript  $m$  and are functions of  $\mathbf{x}$  and  $t$ . However, in subsequent equations these explicit function dependencies may be omitted for brevity. The weighting function  $g(\mathbf{y}, \mathbf{x})$  in (9)–(10) quantifies the relative contribution to the definition of a macroscopic quantity at  $\mathbf{y}$  of all microscopic points  $\mathbf{x}$  in the vicinity of  $\mathbf{y}$ . This function is assumed continuous and has the following properties: (i)  $\int_{\mathcal{R}} g(\mathbf{y}, \mathbf{x}) dv^m = 1$ ; (ii)  $L_m \ll \text{supp } g \ll [\text{vol}(\mathcal{R})]^{1/3}$ , where “supp” denotes the support of a function and  $L_m$  denotes a characteristic microstructural length; (iii)  $g(\mathbf{y}, \mathbf{x}) = 0$  on  $\partial\mathcal{R}$  when  $\mathbf{y} \in \mathcal{R}$ ; and (iv)  $g(\mathbf{y}, \mathbf{x})$  attains a maximum when  $\mathbf{x} = \mathbf{y}$ . Assumption (i) enforces consistency in the averaging definitions (9)–(10); (ii) and (iv) signify the local nature of the macroscopic quantities; finally, (iii) implies that  $g(\mathbf{y}, \mathbf{x})$  affects interior averaging only. Additionally, as argued in [16], invariance of  $g(\mathbf{y}, \mathbf{x})$  under superposed rigid-body motions implies that

$$\frac{\partial}{\partial \mathbf{x}} g(\mathbf{y}, \mathbf{x}) = -\frac{\partial}{\partial \mathbf{y}} g(\mathbf{y}, \mathbf{x}). \quad (11)$$

Starting with the balance laws, it can be shown [16] with the aid of (1), (10) and the properties of the weighting function that the mass balance equation (9) yields the local form of spatial mass balance, which implies consistency of the homogenization.

Proceeding to linear momentum balance, it can be shown [16] that taking the material time derivative of both sides of Eq. (10), using the Reynolds transport theorem and the chain rule, and appealing to the homogenization Eqs. (9)–(10), the properties of the function  $g(\mathbf{y}, \mathbf{x})$  and Eq. (4), the macroscopic body force is given as the volume average of its microscopic counterpart,

$$\rho^M \mathbf{b}^M = \int_{\mathcal{R}} \rho^m \mathbf{b}^m g(\mathbf{y}, \mathbf{x}) dv^m. \quad (12)$$

Likewise, the macroscopic Cauchy stress is defined as

$$\mathbf{T}^M = \int_{\mathcal{R}} \left[ \mathbf{T}^m - \rho^m (\mathbf{v}^m - \mathbf{v}^M) \otimes (\mathbf{v}^m - \mathbf{v}^M) \right] g(\mathbf{y}, \mathbf{x}) dv^m. \quad (13)$$

An analogous approach may be taken using the balance equations in referential form. In this case, with the referential weighting function  $g_0$  defined as  $g_0 = J^M g$ , where  $J^M = \det \mathbf{F}^M$  and  $\mathbf{F}^M$  is the macroscopic deformation gradient, the macroscopic first Piola–Kirchhoff stress is determined to be [16]

$$\begin{aligned} \mathbf{P}^M &= J^M \left[ \int_{\mathcal{R}_0} \left[ \mathbf{P}^m \mathbf{F}^{mT} - \rho_0^m (\mathbf{v}^m - \mathbf{v}^M) \otimes (\mathbf{v}^m - \mathbf{v}^M) \right] g(\mathbf{y}, \mathbf{x}) dV^m \right] \mathbf{F}^{M-T} \\ &= J^M \mathbf{T}^M \mathbf{F}^{M-T}. \end{aligned} \quad (14)$$

A significant consequence of the relations (13)–(14) is that the macroscopic stress explicitly accounts for the influence of micro-inertia through the fluctuations in microscopic velocity. This is consistent with the relations set forth by Irving and Kirkwood [17] in deriving macroscopic stresses from atomistic quantities. It is also important to note that relations (13)–(14) are derived by comparing terms which are operated on by divergences  $\frac{\partial}{\partial \mathbf{y}}$  and  $\frac{\partial}{\partial \mathbf{Y}}$ , respectively.

Hence, these formulae hold *to within a divergence-free term*. As argued in [16], these divergence-free terms may be set to zero as long as the boundary conditions and balance laws at both scales are satisfied simultaneously.

### 2.3. Relation to the Hill–Mandel homogenization method

Motivated by an energy conservation across scales, the Hill–Mandel criterion requires that

$$\mathbf{P}^M \cdot \mathbf{F}^M = \frac{1}{V} \int_{\omega_0} \mathbf{P}^m \cdot \mathbf{F}^m dV^m, \quad (15)$$

where  $\omega_0$  represents the referential domain of an RVE with volume  $V$ , which is associated with a macroscopic material point  $M$ . In addition, the criterion assumes that the deformation gradient and stress in the two scales relate as

$$\mathbf{F}^M = \frac{1}{V} \int_{\omega_0} \mathbf{F}^m dV^m = \bar{\mathbf{F}} \quad (16)$$

and

$$\mathbf{P}^M = \frac{1}{V} \int_{\omega_0} \mathbf{P}^m dV^m = \bar{\mathbf{P}}, \quad (17)$$

where  $\bar{\mathbf{F}}$  and  $\bar{\mathbf{P}}$  denote volume averages of  $\mathbf{F}^m$  and  $\mathbf{P}^m$  over  $\omega_0$ . Finally, scale separation arguments are invoked to deduce that microscopic body forces and inertia effects are negligible in the microscale, leading to fine-scale linear momentum balance in the form

$$\text{Div } \mathbf{P}^m = \mathbf{0}. \quad (18)$$

In essence, Hill–Mandel homogenization aims to impose the energy condition (15) subject to the conditions described in Eqs. (16)–(18). However, these conditions do not hold for arbitrarily loaded RVEs. Rather, special boundary conditions are typically employed (see, e.g., [5,13]) to satisfy Eqs. (15)–(18). These are displacement, traction or periodic boundary conditions on  $\partial\omega_0$ , expressed, respectively, as

$$\mathbf{x}^m = \mathbf{F}^M \mathbf{X}^m, \quad (19)$$

$$\mathbf{p}^m = \mathbf{P}^M \mathbf{N}^m, \quad (20)$$

and

$$\mathbf{x}^+ - \mathbf{x}^- = \mathbf{F}^M (\mathbf{X}^+ - \mathbf{X}^-), \quad \mathbf{p}^+ = -\mathbf{p}^-. \quad (21)$$

The “+” and “−” symbols used in the periodic boundary conditions of Eq. (21) denote quantities linked via periodicity on opposite faces of a periodically deforming RVE, as shown in Fig. 2. Variations to these boundary conditions have also been considered [18].

In contrast to the Hill–Mandel approach, the Irving–Kirkwood continuum homogenization theory does not depend on *a priori* assumptions of the macroscale deformation and stress as volume averages of their microscale counterparts or quasi-static conditions in the microscale. An implication of this less restrictive framework is that the proposed method does not require special boundary conditions on  $\partial\omega_0$ . Still, as demonstrated in [16], an equation identical in form to (15) may be derived from the proposed homogenization theory under a reasonable set of assumptions, indicating that the Hill–Mandel theory is simply a subset of the more general continuum Irving–Kirkwood theory. In closing, it is important to stress that the Hill–Mandel condition (15) does not, in general, constitute a statement of energy conservation across the two scales, since the dot-product of the first Piola–Kirchhoff stress and the deformation gradient is not equal to (twice) the internal energy of the system, except for the very special case of infinitesimal elastic deformations.

### 3. Novel finite element multiscale problem formulations

The continuum Irving–Kirkwood theory discussed in Section 2 allows for greater freedom in the formulation of RVE boundary-value problems when compared to the Hill–Mandel homogenization method. As such, it is of interest

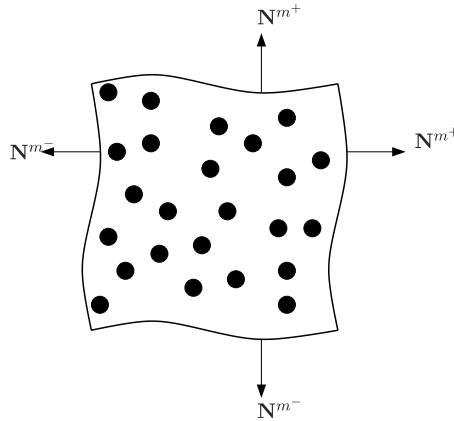


Fig. 2. RVE deforming under periodic boundary conditions.

to develop RVE problem formulations which deviate from the Hill–Mandel method for continuum homogenization. This section explores alternative RVE boundary-value problem formulations compatible with the continuum Irving–Kirkwood theory discussed in Section 2, and describes their finite element implementation. The only prerequisite for the selection of such boundary conditions is that they relay to the microscale sufficient information on the local macroscopic deformation. To this end, boundary-value problems are formulated which require that the deformation gradient or strain at the macroscale be taken as the volume-average of the corresponding quantity over the microscale. While this is not the only way that one may relate deformation between scales, it is perhaps one of the most natural, given the focus on volume-averaging promoted by the continuum Irving–Kirkwood theory.

The principal assumptions adopted throughout this section and the rest of this article are that all processes are purely mechanical and quasi-static.

### 3.1. A mixed boundary-value problem for the RVE based on deformation gradient averaging

By way of background, recall that when imposing constant traction boundary conditions, as in (20), the prescribed average deformation gradient condition (16) may be additionally enforced on the RVE using Lagrange multipliers, as originally suggested in [6,15]. In particular, traction boundary conditions of the form (20) trivially imply that (17) holds. In addition, the Hill–Mandel energy condition (15) is recovered by contracting the constraint condition (16) with  $\mathbf{P}^M$  and using (20), therefore

$$\mathbf{P}^M \cdot \left[ \frac{1}{V} \int_{\omega_0} \mathbf{F}^m dV^m - \mathbf{F}^M \right] = 0. \quad (22)$$

This, in turn, implies that  $\mathbf{P}^M$  may be interpreted as a Lagrange multiplier that enforces (16).

Returning to the general setting of Irving–Kirkwood homogenization, it is possible to formulate a mixed boundary-value problem for the microscale as

$$\text{Div } \mathbf{P}^m + \rho_0^m \mathbf{b}^m = \mathbf{0} \quad \text{in } \omega_0, \quad (23)$$

$$\mathbf{x}^m = \mathbf{F}^M \mathbf{X}^m \quad \text{on } \Gamma_u, \quad (24)$$

$$\mathbf{p}^m = \mathbf{0} \quad \text{on } \Gamma_q, \quad (25)$$

subject to the prescribed average deformation gradient constraint condition (16), which will be enforced with Lagrange multipliers  $\mathbf{A}$ . Here, displacement and traction boundary conditions are respectively imposed on  $\Gamma_u$  and  $\Gamma_q$ , and  $\partial\omega_0 = \overline{\Gamma_u} \cup \overline{\Gamma_q}$ . The conditions (24) and (16) may be viewed as passing information on the macroscopic deformation to the microscale. The homogeneous condition in (25) reflects the fact that no prescribed external traction is imposed on  $\Gamma_q$  at the outset. However, in analogy to the preceding constant traction problem, a non-zero traction is generated on  $\Gamma_q$  by the multipliers due to the enforcement of the constraint condition (16).

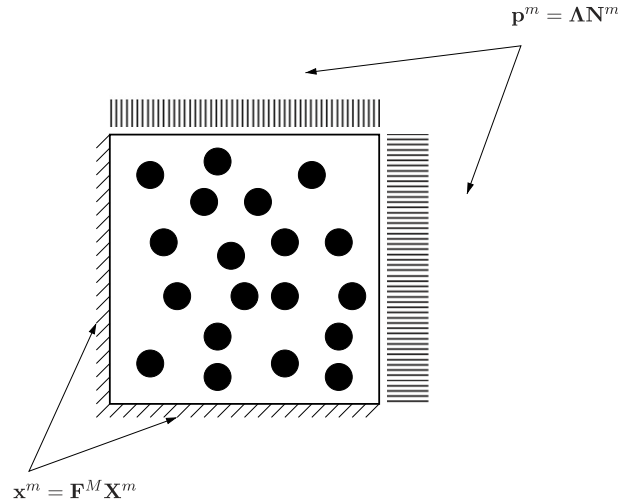


Fig. 3. RVE subjected to mixed traction and displacement boundary conditions resulting from imposing  $\mathbf{F}^M = \bar{\mathbf{F}}$ .

While this formulation prescribes the average deformation gradient in the RVE to be  $\mathbf{F}^M$ , it relaxes the requirement that  $\mathbf{P}^M = \bar{\mathbf{P}}$  by using the stress homogenization formula (14), and also explicitly accounts for body forces in the microscale. Hence, the boundary-value problem defined by (23)–(25) and (16) represents a deviation from the Hill–Mandel method, and a generalized version of the constant traction problem considered in [6,15].

The weak (virtual work-based) form of the proposed boundary-value problem takes the form

$$\int_{\omega_0} \delta \mathbf{F}^m \cdot (\mathbf{P}^m - \mathbf{\Lambda}) dV^m + \int_{\omega_0} \delta \mathbf{\Lambda} \cdot (\mathbf{F}^M - \mathbf{F}^m) dV^m = \int_{\omega_0} \rho_0^m \mathbf{b}^m \cdot \delta \mathbf{u}^m dV^m, \quad (26)$$

where  $\delta \mathbf{u}^m$  denotes the virtual displacement,  $\delta \mathbf{F}^m = \frac{\partial \delta \mathbf{u}^m}{\partial \mathbf{X}}$  the corresponding virtual deformation gradient,  $\mathbf{\Lambda}$  the Lagrange multiplier enforcing (16) and  $\delta \mathbf{\Lambda}$  the corresponding virtual multiplier. Note that the constraint (16) is global in nature, that is, it applies to the RVE as a whole rather than to individual points. Also, the same constraint is workless, since

$$\int_{\omega_0} \mathbf{\Lambda} \cdot \delta \mathbf{F}^m dV^m = \int_{\omega_0} \mathbf{\Lambda} \cdot \delta (\mathbf{F}^m - \mathbf{F}^M) dV^m = \mathbf{\Lambda} \cdot \delta \int_{\omega_0} (\mathbf{F}^m - \mathbf{F}^M) dV^m = 0, \quad (27)$$

given the constancy of  $\mathbf{F}^M$  and  $\mathbf{\Lambda}$  in  $\omega_0$ , see [19, Section 30] for a discussion of worklessness in the context of a theory of internal constraints.

Next, starting from the virtual work done by the Lagrange multiplier term in (26), one may deduce with the aid of the divergence theorem that

$$\int_{\omega_0} \mathbf{\Lambda} \cdot \delta \mathbf{F}^m dV^m = \int_{\partial \omega_0} \mathbf{\Lambda} \cdot (\delta \mathbf{u}^m \otimes \mathbf{N}^m) dA^m = \int_{\Gamma_q} (\mathbf{\Lambda} \mathbf{N}^m) \cdot \delta \mathbf{u}^m dA^m. \quad (28)$$

This demonstrates that the Lagrange multipliers effectively contribute a traction  $\mathbf{p}^m = \mathbf{\Lambda} \mathbf{N}^m$  on the boundary  $\Gamma_q$ . This is the traction required on  $\Gamma_q$  to satisfy the internal constraint (16) given the boundary-value problem described by (23)–(25). The resulting effective boundary conditions on the RVE are depicted schematically in Fig. 3.

To proceed with a finite element solution of the RVE problem, a standard interpolation of the displacement components  $u_a^m$  is introduced as

$$u_a^m = \sum_{K=1}^N \phi_K \hat{u}_a^K, \quad (29)$$

where  $\phi_K$  is the finite element interpolation function for node  $K$  and  $N$  is the number of nodes in the finite element mesh. The notation  $(\hat{\cdot})$  is used to signify nodal values. Substituting (29) into Eq. (26) and exploiting the arbitrariness

of the variations  $\delta u_a^m$  and  $\delta \Lambda_{aA}$  yields the equations

$$R_a^K = \int_{\omega_0} P_{aA}^m \frac{\partial \phi_K}{\partial X_A} dV^m - \Lambda_{aA} \int_{\omega_0} \frac{\partial \phi_K}{\partial X_A} dV^m - \int_{\omega_0} \rho_0^m b_a^m \phi_K dV^m = 0 \quad (30)$$

and

$$r_{aA} = \int_{\omega_0} (F_{aA}^M - F_{aA}^m) dV^m = 0, \quad (31)$$

where the standard summation convention over repeated Cartesian indices is employed. Since Eq. (30) is generally nonlinear in  $\hat{u}_a^K$ , a Newton–Raphson method may be employed for the solution of the system of (30) and (31). Taking the differential of (30) in the direction  $(d\hat{u}_b^L, d\Lambda_{bB})$  leads to

$$dR_a^K = \sum_{L=1}^N (C_{ab}^{KL} d\hat{u}_b^L) + G_{a,bB}^K d\Lambda_{bB}. \quad (32)$$

In Eq. (32),  $C_{ab}^{KL}$  results from differentiating the stress-divergence term in (30), while  $G_{a,bB}^K$  is defined as

$$G_{a,bB}^K = -\delta_{ab} \int_{\omega_0} \frac{\partial \phi_K}{\partial X_B} dV^m, \quad (33)$$

where  $\delta_{ab}$  is the Kronecker delta and the comma in the subscript is intended to distinguish between rows and columns in a matrix representation. Next, taking the differential of (31) gives rise to

$$dr_{aA} = V dF_{aA}^M + \sum_{L=1}^N G_{aA,b}^L d\hat{u}_b^L, \quad (34)$$

where the term  $dF_{aA}^M$  is explicitly retained (although it vanishes during the solution of the RVE boundary-value problem) to reflect the coupling of the two scales in the ensuing algorithmic treatment (see Appendix A.1). Also note that the matrix  $G_{aA,b}^L$  in (34) represents the transpose of the matrix  $G_{b,aA}^L$  in (32).

A Newton–Raphson procedure in the microscale (where  $F_{aA}^M$  is prescribed), may now be employed by using Eqs. (32) and (34) to generate the system of equations

$$\begin{bmatrix} C_{ab}^{KL} & G_{a,bB}^K \\ G_{cC,b}^L & 0 \end{bmatrix} \begin{bmatrix} \Delta \hat{u}_b^L \\ \Delta \Lambda_{bB} \end{bmatrix} = \begin{bmatrix} -\tilde{R}_a^K \\ -r_{cC} \end{bmatrix}, \quad (35)$$

from where one may iteratively solve for the increments  $\Delta \hat{u}_b^L$  and  $\Delta \Lambda_{bB}$ . Note that, with a slight abuse of notation,  $C_{ab}^{KL}$ ,  $\hat{u}_b^L$ , etc. in Eq. (35) denote matrices of all components rather than individual components of the respective quantities.

An important point here concerns the minimum number of degrees of freedom that need to be specified according to (24) in order to render the matrix in (35) non-singular. These degrees of freedom are meant to restrain the body from undertaking a rigid body motion. To deduce this minimum number, note that the prescription of the average deformation gradient by (16) eliminates any arbitrariness in rigid body rotation. To show this, assume that an average deformation equal to  $\mathbf{F}^M$  corresponds to two deformation gradient fields  $\mathbf{F}^m$  and  $\mathbf{F}^{m'}$  that differ by a rigid body rotation  $\mathbf{R}^m$ . Therefore  $\mathbf{F}^{m'} = \mathbf{R}^m \mathbf{F}^m$ , where  $\mathbf{R}^m$  is constant throughout the domain  $\omega_0$ . Given that  $\mathbf{F}^m$  and  $\mathbf{F}^{m'}$  share the same average value, it follows that

$$\bar{\mathbf{F}}^m - \bar{\mathbf{R}}^m \bar{\mathbf{F}}^m = \bar{\mathbf{F}}^m - \bar{\mathbf{R}}^m \bar{\mathbf{F}}^m = \mathbf{0}, \quad (36)$$

hence  $\bar{\mathbf{R}}^m = \mathbf{R}^m = \mathbf{I}$ . Therefore, the boundary conditions (24) are only required to restrain rigid body translations.

Once the microscopic solution has been computed, it is necessary to extract from it the homogenized stress and tangent matrix to be used for the macroscopic solution. The reader is referred to Section 4 and Appendix A.1 for the derivation of the relevant equations for this procedure.



### 3.2. A mixed boundary-value problem for the RVE based on strain averaging

The preceding RVE boundary-value problem was structured as to enforce the average deformation gradient constraint of Eq. (16). However, the continuum Irving–Kirkwood theory in [16] does not require that the deformation be specifically subject to (16). To highlight this point and explore its implications, consider an alternative constraint condition on the deformation, in the form

$$\int_{\omega_0} (\mathbf{E}^M - \mathbf{E}^m) dV^m = \mathbf{0}, \quad (37)$$

where  $\mathbf{E} = \frac{1}{2}(\mathbf{F}^T \mathbf{F} - \mathbf{I})$  is the Lagrangian strain tensor, and  $\mathbf{E}^m$  and  $\mathbf{E}^M$  are its microscopic and macroscopic counterparts, respectively.

Consider now the weak form of the mixed boundary-value problem described in Eqs. (23)–(25), but this time subject to the strain-averaging constraint (37). Appealing to the same procedure as in Section 3.1, the weak form may be deduced as

$$\int_{\omega_0} \delta \mathbf{F}^m \cdot \mathbf{P}^m dV^m - \int_{\omega_0} \boldsymbol{\lambda} \cdot \delta \mathbf{E}^m dV^m + \int_{\omega_0} \delta \boldsymbol{\lambda} \cdot (\mathbf{E}^M - \mathbf{E}^m) dV^m = \int_{\omega_0} \rho_0^m \mathbf{b}^m \cdot \delta \mathbf{u}^m dV^m. \quad (38)$$

Here, the spatially homogeneous Lagrange multiplier  $\boldsymbol{\lambda}$  is represented as a symmetric tensor, corresponding to the symmetric tensor-valued constraint (37) and reflecting the fact that only six unique constraints exist due to the symmetry of  $\mathbf{E}$ . Upon writing  $\delta \mathbf{E}^m = \frac{1}{2}(\delta \mathbf{F}^m T \mathbf{F}^m + \mathbf{F}^{mT} \delta \mathbf{F}^m)$  and taking advantage of the symmetries of  $\mathbf{E}$  and  $\boldsymbol{\lambda}$ , Eq. (38) may be rewritten analogously to (26) as

$$\int_{\omega_0} \delta \mathbf{F}^m \cdot (\mathbf{P}^m - \mathbf{F}^m \boldsymbol{\lambda}) dV^m + \int_{\omega_0} \delta \boldsymbol{\lambda} \cdot (\mathbf{E}^M - \mathbf{E}^m) dV^m = \int_{\omega_0} \rho_0^m \mathbf{b}^m \cdot \delta \mathbf{u}^m dV^m. \quad (39)$$

As in the average deformation gradient case, the constraint (37) is workless, since, owing to (37) and the constancy of  $\mathbf{E}^M$  and  $\boldsymbol{\lambda}$  in  $\omega_0$ ,

$$\int_{\omega_0} \boldsymbol{\lambda} \cdot \delta \mathbf{E}^m dV^m = \int_{\omega_0} \boldsymbol{\lambda} \cdot \delta (\mathbf{E}^m - \mathbf{E}^M) dV^m = \boldsymbol{\lambda} \cdot \delta \int_{\omega_0} (\mathbf{E}^m - \mathbf{E}^M) dV^m = 0. \quad (40)$$

Starting from the work-like quantity on left-hand side of (40), a physical interpretation of the multiplier  $\boldsymbol{\lambda}$  may be obtained by using integration by parts and the divergence theorem, while also exploiting the symmetry of  $\boldsymbol{\lambda}$  and  $\mathbf{E}^m$ . This, by way of integration-by-parts and the divergence theorem, leads to

$$\begin{aligned} \int_{\omega_0} \boldsymbol{\lambda} \cdot \delta \mathbf{E}^m dV^m &= \int_{\omega_0} \mathbf{F}^m \boldsymbol{\lambda} \cdot \delta \mathbf{F}^m dV^m \\ &= \int_{\Gamma_q} (\mathbf{F}^m \boldsymbol{\lambda} \mathbf{N}^m) \cdot \delta \mathbf{u}^m dA^m - \int_{\omega_0} \left[ \frac{\partial \mathbf{F}^m}{\partial \mathbf{X}} \boldsymbol{\lambda} \right] \cdot \delta \mathbf{u}^m dV^m, \end{aligned} \quad (41)$$

where, for clarity, it is noted that  $\left[ \frac{\partial \mathbf{F}^m}{\partial \mathbf{X}} \boldsymbol{\lambda} \right]$  is a vector resulting from the contraction of the third-order tensor  $\frac{\partial \mathbf{F}^m}{\partial \mathbf{X}}$  and the second-order tensor  $\boldsymbol{\lambda}$ . In view of (38) and (41), the multiplier  $\boldsymbol{\lambda}$  effectively contributes a traction  $\mathbf{p}^m = (\mathbf{F}^m \boldsymbol{\lambda}) \mathbf{N}^m$  on  $\Gamma_q$ , although, unlike the average deformation gradient case, this traction is not constant, but rather varies with  $\mathbf{F}^m$ . Eq. (41) also implies that the multiplier contributes a body force-like term which varies with the gradient of  $\mathbf{F}^m$  over the domain  $\omega_0$ . These effective contributions by the multiplier are depicted schematically in Fig. 4.

Introducing the finite element interpolation (29) and invoking the arbitrariness of the variations, Eq. (39) gives rise to

$$\tilde{R}_a^K = \int_{\omega_0} P_{aA}^m \frac{\partial \phi_K}{\partial X_A} dV^m - \int_{\omega_0} \rho_0^m b_a^m \phi_K dV^m - \frac{1}{2} \lambda_{AB} \int_{\omega_0} \left( F_{aA}^m \frac{\partial \phi_K}{\partial X_B} + F_{aB}^M \frac{\partial \phi_K}{\partial X_A} \right) dV^m = 0 \quad (42)$$

and

$$\tilde{r}_{AB} = \int_{\omega_0} \left( E_{AB}^M - \frac{1}{2} (F_{aA}^m F_{aB}^m - \delta_{AB}) \right) dV^m = 0. \quad (43)$$

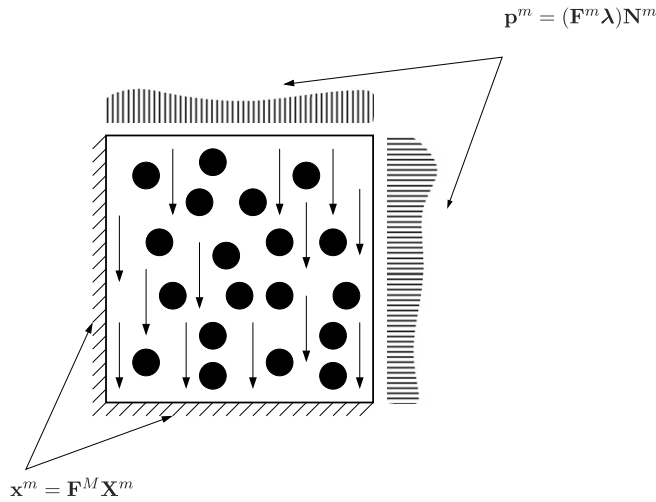


Fig. 4. RVE subjected to mixed traction and displacement boundary conditions resulting from imposing  $\mathbf{E}^M = \bar{\mathbf{E}}$  (the downward arrows represent the additional effective body force generated from imposing the constraint).

To employ a Newton–Raphson method for the solution of (42) and (43), start by taking the differential of (42) in the direction  $(d\hat{u}_b^L, d\lambda_{AB})$ , which leads to

$$d\tilde{R}_a^K = \sum_{L=1}^N \tilde{C}_{ab}^{KL} d\hat{u}_b^L + \tilde{G}_{a,AB}^K d\lambda_{AB}, \quad (44)$$

where the matrices  $\tilde{C}_{ab}^{KL}$  and  $\tilde{G}_{a,AB}^L$  are defined by

$$\tilde{C}_{ab}^{KL} = C_{ab}^{KL} - \frac{1}{2} \lambda_{AB} \delta_{ab} \int_{\omega_0} \left( \frac{\partial \phi_K}{\partial X_A} \frac{\partial \phi_L}{\partial X_B} + \frac{\partial \phi_K}{\partial X_B} \frac{\partial \phi_L}{\partial X_A} \right) dV^m \quad (45)$$

and

$$\tilde{G}_{b,AB}^K = -\frac{1}{2} \int_{\omega_0} \left( F_{bA}^m \frac{\partial \phi_K}{\partial X_B} + F_{bB}^m \frac{\partial \phi_K}{\partial X_A} \right) dV^m. \quad (46)$$

Next, taking the differential of Eq. (43) gives

$$d\tilde{r}_{AB} = V dE_{AB}^M + \sum_{L=1}^N \tilde{G}_{b,AB}^L d\hat{u}_b^L, \quad (47)$$

where the matrix  $\tilde{G}_{b,AB}^L$  represents the transpose of the matrix  $\tilde{G}_{AB,b}^L$ . It follows that, for each Newton–Raphson iteration in the microscale (where,  $E_{AB}^M$  is prescribed), Eqs. (44) and (47) can be used to derive a system which is expressed in matrix form as

$$\begin{bmatrix} \tilde{C}_{ab}^{KL} & \tilde{G}_{a,AB}^K \\ \tilde{G}_{CD,b}^L & 0 \end{bmatrix} \begin{bmatrix} \Delta \hat{u}_b^L \\ \Delta \lambda_{AB} \end{bmatrix} = \begin{bmatrix} -\tilde{R}_a^K \\ -\tilde{r}_{CD} \end{bmatrix}. \quad (48)$$

The displacement boundary conditions (24) for this boundary-value problem need to explicitly restrain both rigid body translations and rotations. The need to restrain the rigid body rotations stems from the observation that any two deformation gradient fields  $\mathbf{F}^m$  and  $\mathbf{F}^{m'} = \mathbf{R}^m \mathbf{F}^m$  that differ by a rigid rotation  $\mathbf{R}^m$  would generate the same average Lagrangian strain  $\bar{\mathbf{E}}^m$ .

The reader may refer to Section 4 and Appendix A.2 for the details of the homogenization of the stress and tangent matrix resulting from this RVE boundary-value problem.

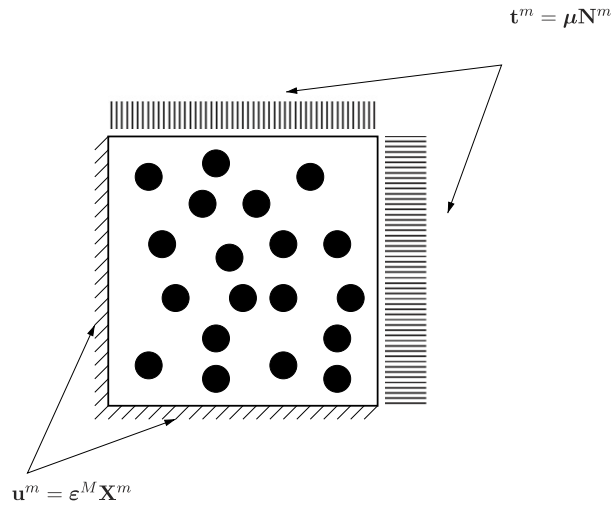


Fig. 5. RVE subjected to mixed traction and displacement boundary conditions resulting from imposing  $\epsilon^M = \bar{\epsilon}$ .

### 3.3. A formulation for infinitesimal deformations

The two microscale boundary-value problems discussed thus far involve finite deformations. For completeness, a formulation for infinitesimal deformation models (e.g., linear elasticity) is derived here based on the strain averaging approach of Section 3.2. Letting the infinitesimal strain tensor be defined as  $\epsilon = \frac{1}{2} \left( \frac{\partial \mathbf{u}}{\partial \mathbf{X}} + \left( \frac{\partial \mathbf{u}}{\partial \mathbf{X}} \right)^T \right)$ , the linearized counterpart of the constraint (37) on the RVE is cast as

$$\int_{\omega_0} (\epsilon^M - \epsilon^m) dV^m = \mathbf{0}. \quad (49)$$

The resulting RVE boundary-value problem is then given by

$$\text{Div } \sigma^m + \rho_0^m \mathbf{b}^m = \mathbf{0} \quad \text{in } \omega_0, \quad (50)$$

$$\mathbf{u}^m = \frac{\partial \mathbf{u}^M}{\partial \mathbf{X}} \mathbf{X}^m \quad \text{on } \Gamma_u, \quad (51)$$

$$\mathbf{t}^m = \mathbf{0} \quad \text{on } \Gamma_q, \quad (52)$$

where  $\partial \omega_0 = \overline{\Gamma_u \cup \Gamma_q}$ ,  $\sigma$  denotes the stress tensor for the case of infinitesimal deformations, and the deformation must satisfy the constraint given by Eq. (49). Once again, the homogeneous traction boundary condition reflects the fact that no external loading is prescribed to the RVE on  $\Gamma_q$ . Note that the Dirichlet boundary conditions (51) simplify to

$$\mathbf{u}^m = \epsilon^M \mathbf{X}^m \quad \text{on } \Gamma_u, \quad (53)$$

provided that the stress is independent of the infinitesimal rotation  $\omega = \frac{1}{2} \left( \frac{\partial \mathbf{u}}{\partial \mathbf{x}} - \left( \frac{\partial \mathbf{u}}{\partial \mathbf{x}} \right)^T \right)$ , as is typically the case in constitutive modeling.

In analogy to the RVE constraint formulations for the finite deformation case, the weak form of the boundary-value problem (50)–(52) may be expressed as

$$\int_{\omega_0} \delta \epsilon^m \cdot (\sigma^m - \mu) dV^m + \int_{\omega_0} \delta \mu \cdot (\epsilon^M - \epsilon^m) dV^m = \int_{\omega_0} \rho_0^m \mathbf{b}^m \cdot \delta \mathbf{u}^m dV^m, \quad (54)$$

where  $\mu$  is the Lagrange multiplier enforcing the constraint condition (49). Following closely the development in Sections 3.1 and 3.2, it can be easily shown that the constraint (49) is workless, and that the Lagrange multipliers used to enforce it generate an effective traction  $\mathbf{t}^m = \mu \mathbf{N}^m$  applied to  $\Gamma_q$  on the RVE boundary. The resulting effective RVE boundary conditions are schematically depicted in Fig. 5.

Substituting the interpolated finite element displacement (29) into Eq. (54) and invoking arbitrariness of the variations in displacements and multipliers results in

$$\int_{\omega_0} \sigma_{ab}^m \frac{\partial \phi_K}{\partial X_b} dV^m - \mu_{ab} \int_{\omega_0} \frac{\partial \phi_K}{\partial X_b} dV^m = \int_{\omega_0} \rho_0^m b_a^m \phi_K dV^m \quad (55)$$

and

$$\int_{\omega_0} \varepsilon_{ab}^m dV^m = V \varepsilon_{ab}^M. \quad (56)$$

Since the system of equations (55) and (56) is linear in both  $\hat{\mathbf{u}}$  and  $\boldsymbol{\mu}$ , it may be expressed in matrix form as

$$\begin{bmatrix} \check{C}_{ab}^{KL} & \check{G}_{a,ef}^K \\ \check{G}_{ef,b}^L & 0 \end{bmatrix} \begin{bmatrix} \hat{u}_b^L \\ \mu_{ef} \end{bmatrix} = \begin{bmatrix} \check{R}_a^K \\ -V \varepsilon_{ef}^M \end{bmatrix}, \quad (57)$$

where

$$\check{G}_{a,mn}^K = -\frac{1}{2} \int_{\omega_0} \left( \frac{\partial \phi_K}{\partial X_m} \delta_{af} + \frac{\partial \phi_K}{\partial X_n} \delta_{ae} \right) dV^m. \quad (58)$$

Also,  $\check{R}_a^K$  represents the contribution of any body forces present in the problem, and  $\check{C}_{ab}^{KL}$  is the stiffness matrix associated with the representation of the stress-divergence term in (55) as a linear function of  $\hat{\mathbf{u}}$ . As with the boundary-value problem in Section 3.2, this system has a unique solution if sufficient displacement boundary conditions are specified to restrain both rigid translations and rotations. The reader may refer to Section 4 and Appendix A.3 for the details of the homogenization of the stress and tangent matrix resulting from this RVE boundary-value problem.

#### 4. Stress homogenization and numerical examples

Traditional implementations of FE<sup>2</sup> stress homogenization based on the Hill–Mandel criterion take advantage of the divergence-free microscopic stress state to convert the volume integral defining the macroscopic stress to an equivalent surface integral [5,6,15]. This is clearly not possible for the general definition of macroscopic stress in (13). Therefore, stress homogenization will be effected here using volume integration over the RVE.

With reference to the continuum Irving–Kirkwood theory in Section 2,  $g(\mathbf{y}, \mathbf{x})$  is taken here to be a box function, that is,

$$g(\mathbf{y}, \mathbf{x}) = \begin{cases} \frac{1}{v} & \text{if } \mathbf{x} \in \omega \\ 0 & \text{if } \mathbf{x} \notin \omega. \end{cases} \quad (59)$$

In addition, for consistency with the proposed multiscale formulations in Section 3, all processes are assumed to be purely mechanical and quasi-static. Note that piecewise continuity of the box function in (59) is a sufficient restriction on  $g$  for the purpose of deriving the macroscopic stress formulae (13) and (14).

Starting from (13), neglecting the fluctuations of microscale velocity relative to the macroscale, and taking into account the weighting function in (59) leads to

$$\mathbf{T}^M = \frac{1}{v} \int_{\omega} \mathbf{T}^m dv^m. \quad (60)$$

Likewise, starting from (14), one finds that

$$\mathbf{P}^M = \frac{J^M}{v} \left[ \int_{\omega_0} \mathbf{P}^m \mathbf{F}^{mT} dV^m \right] \mathbf{F}^{M-T}. \quad (61)$$

Standard Gaussian integration is employed to compute these integrals over the RVE domain.

Note that, unlike the case of internally constrained materials (e.g., incompressible elastic solids), the Lagrange multipliers used in Section 3.1–3.3 are global (reflecting the global nature of the imposed constraints). Therefore,

Table 1

Young's moduli  $E_i$  (in GPa), Poisson's ratios and shear moduli  $G_{ij}$  (in GPa) for the orthotropic Kirchhoff–Saint Venant solid.

	$E_1$	$E_2$	$E_3$	$\nu_{12}$	$\nu_{23}$	$\nu_{31}$	$G_{12}$	$G_{23}$	$G_{31}$
Core	300	200	150	0.35	0.33	0.24	111	75.2	60.5
Matrix	10	20	30	0.20	0.33	0.30	4.17	7.52	11.5

Table 2

Euler angles and probabilities describing the orientation of orthotropic crystals in the core and matrix regions.

	$\alpha$	$\beta$	$\gamma$	Probability
Core 1	45	30	20	0.5
Core 2	−45	0	60	0.5
Matrix 1	−30	30	45	0.25
Matrix 2	15	30	45	0.75

these multipliers are not directly added to the microscopic stress, but rather contribute to the deformation resulting in the constitutively determined microscopic stress  $\mathbf{T}^m$  that enters (60).

The remainder of this section focuses on two numerical examples which are intended to evaluate the performance of the RVE problem formulations developed in Section 3 and to compare it to performance of the Hill–Mandel formulations. The latter typically employ the displacement, traction, or periodic RVE boundary conditions in Eqs. (19)–(21). It has been well documented that the choice of RVE boundary conditions influences the homogenized material stiffness response (see, e.g. [5]). In particular, with respect to the material stiffness, displacement conditions give an upper bound, traction conditions give a lower bound, and periodic conditions yield a response in between these bounds. Hence, the deformation prescribed to an RVE directly influences the results of a finite element homogenization procedure. With this point under consideration, two numerical examples are employed to demonstrate the response obtained by the newly proposed RVE boundary conditions, and the results compared to those obtained by corresponding Hill–Mandel RVE problem formulations.

All computations are performed using a version of the general-purpose finite element program FEAP [20–22] which allows for parallel implementation of  $\text{FE}^2$  methods using the *Open MPI* [23] version of the classical Message Passing Interface.

#### 4.1. Polycrystalline elastic cantilever beam in plane strain

This example seeks to evaluate how the choice of RVE boundary conditions in the  $\text{FE}^2$  method influences the homogenized stiffness response of the material in the macroscale. To this end, an idealized material is constructed whose microstructure consists of a repeating pattern of orthotropic crystals at different orientations. The individual crystals in the microscale are assumed to behave according to the nonlinearly elastic Kirchhoff–Saint Venant constitutive law  $\mathbf{S} = \mathbb{C}\mathbf{E}$ , where  $\mathbf{S} = \mathbf{F}^{-1}\mathbf{P}$  is the second Piola–Kirchhoff stress and  $\mathbb{C}$  is the classical fourth-order orthotropic elasticity tensor.

In order to construct a mesh of the crystalline microstructure in the RVE, a standard modeling strategy is employed whereby each element in the RVE mesh (taken to be of unit size) represents a single crystal with particular material properties and orientation. The crystals are assumed to aggregate into a stiff core with a surrounding soft matrix, as shown in Fig. 6. To facilitate meaningful comparisons, a single RVE is generated using a pseudo-random crystal orientation distribution and is assigned to all material points in the macroscale. The material parameters used in the core and matrix regions are shown in Table 1, and orientation options with corresponding probabilities of occurrence are shown in Table 2.

The problem considered in the macroscale is the bending of a cantilever beam in plane strain, as shown in Fig. 7. Here, the vertical deflection of the top right-corner of the beam is prescribed as  $\bar{u}_2 = -0.02$  m, and the resulting reaction force at the supporting wall is computed. A uniform  $20 \times 4$  mesh of displacement-based 4-node quadrilateral elements with  $2 \times 2$  integration is used in the macroscale, while a  $12 \times 12$  mesh of like elements is used in the RVE of the microscale, as in Fig. 6. The problem is solved for a variety of RVE boundary conditions, including those

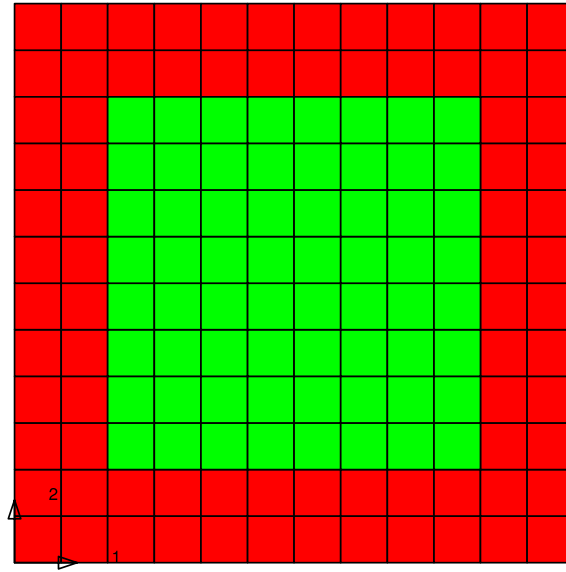


Fig. 6. Finite element mesh (144 elements in total) for an RVE consisting of orthotropic crystals. Green elements represent the stiffer crystals, while red elements represent the softer surrounding matrix crystals. (For interpretation of the references to colour in this figure legend, the reader is referred to the web version of this article.)

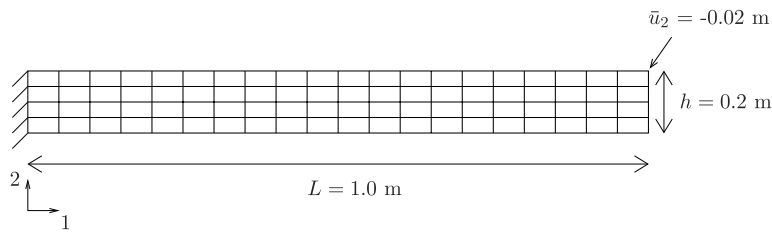


Fig. 7. Bending of a polycrystalline beam: macroscale mesh and boundary conditions.

Table 3  
RVE boundary conditions and their detailed description.

Name	Description
DISP	Displacement
PERI	Periodic
FLBE	$\mathbf{F} = \bar{\mathbf{F}}$ , fixed on left and bottom edge
FLED	$\mathbf{F} = \bar{\mathbf{F}}$ , fixed on left edge
FCOR	$\mathbf{F} = \bar{\mathbf{F}}$ , fixed at corners
FMIN	$\mathbf{F} = \bar{\mathbf{F}}$ , fixed at bottom left corner
ELBE	$\mathbf{E} = \bar{\mathbf{E}}$ , fixed on left and bottom edge
ELED	$\mathbf{E} = \bar{\mathbf{E}}$ , fixed on left edge
ECOR	$\mathbf{E} = \bar{\mathbf{E}}$ , fixed at corners
EMIN	$\mathbf{E} = \bar{\mathbf{E}}$ , fixed at bottom left corner and bottom right corner (vertical only)

compatible with the Hill–Mandel approach, as well as the types of boundary conditions discussed in Section 3. For convenience, Table 3 contains a description of each of the RVE boundary conditions employed in this example.

Fig. 8 depicts the resultant wall reaction force induced by the deflection of the beam for each of the ten RVE boundary conditions in Table 3. As expected, displacement boundary conditions (DISP) yield the stiffest response, while the minimally constraining boundary conditions (FMIN, EMIN) discussed in Sections 3.1 and 3.2 yield the softest responses. The reaction forces between these bounds spans about a 20% difference, indicating the sensitivity

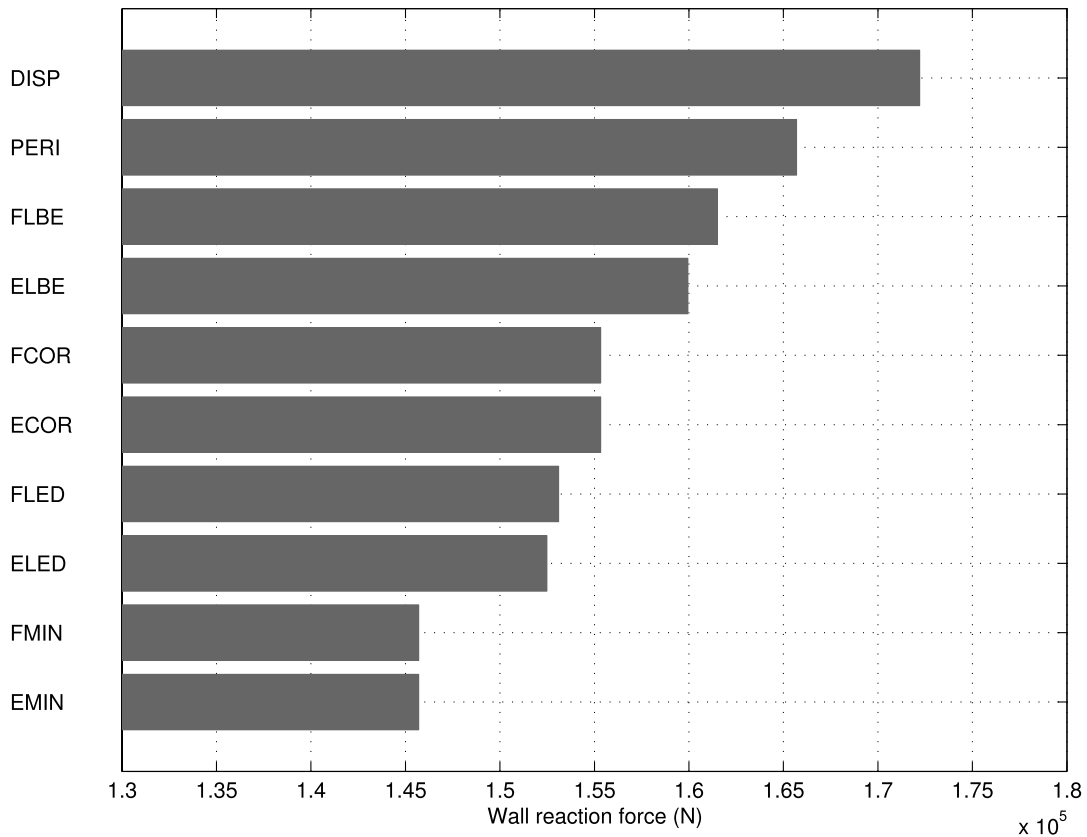


Fig. 8. Bending of a polycrystalline beam: resultant vertical reaction force at the support for different RVE boundary conditions.

of the final answer to the boundary conditions used in the RVE. Also, it is clear from the same figure that the stiffness depends on the fraction and distribution of the RVE boundary that is subject to fixed displacement boundary conditions. In fact, Fig. 8 suggests that there exists a smooth range of stiffness responses between the upper bound (DISP) and lower bound (EMIN) where stiffness increases with the fraction of the fixed RVE boundary and the evenness of its distribution on the four edges. Fig. 8 also demonstrates that the constraint on the average deformation gradient produces slightly stiffer response in all tested boundary conditions than the corresponding constraint on the average Lagrangian strain.

The existence of a rich set of RVE solutions (hence, stiffness responses) is in stark contrast with the limited set of responses permitted by the traditional Hill–Mandel formulation of the RVE problem. This example provides evidence that such additional formulations are not only possible, but also yield reasonable results.

#### 4.2. Uniaxial tension of a composite bar in plane strain

While the preceding example demonstrates that a broad range of possible RVE boundary condition choices exists, it offers no insights as to the accuracy of the predicted stiffness response relative to the exact solution. Here, such an insight is obtained by first solving a problem involving a microstructurally heterogeneous material on a single scale with full resolution of the microstructure. Subsequently, this reference solution is compared to those obtained using  $FE^2$  homogenization with various sets of RVE boundary conditions.

The microstructure comprises of two isotropic linearly elastic material constituents, whose properties are given in Table 4. The constituents are randomly distributed throughout the bar with the same probability of occurrence. Each particle of the two constituents is represented by a single finite element in the single-scale mesh. In particular, all particles are taken to be square in shape with side length  $20 \mu\text{m}$ .

The problem considered here is that of an elastic composite bar undergoing uniaxial tension in plane strain, as shown in Fig. 9. The bar is fixed at its left end, and a constant tensile traction  $\bar{t} = 10 \text{ kPa}$  is applied at its right end.

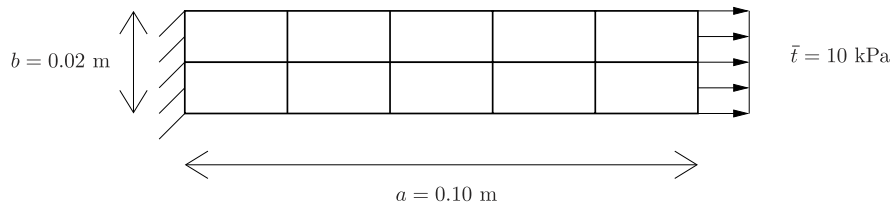


Fig. 9. Tension of a composite bar: macroscale mesh and boundary conditions.

Table 4

Young's moduli (GPa) and Poisson's ratios for the two constituent materials of the composite bar.

	$E$	$\nu$
Constituent 1	1.0	0.30
Constituent 2	3.0	0.35

Table 5

Mean, minimum, maximum, and standard deviation of modulus values (in GPa) for a set of 10 realizations of a  $40 \times 40$  element RVE mesh.

	Mean	Min	Max	St. Dev.
$c_{11}$	2.4986	2.4875	2.5225	0.0112
$c_{22}$	2.4930	2.4807	2.5100	0.0093
$c_{44}$	0.6565	0.6531	0.6607	0.0025
$c_{12}$	1.1306	1.1216	1.1402	0.0061

The average axial displacement is measured at the right end of the bar. The single-scale analysis is conducted on a  $5000 \times 1000$  mesh of 4-node displacement-based elements with  $2 \times 2$  integration. To create the composite material at the macroscale, each element in the mesh has its material properties set to those of either constituent 1 or 2, as in Table 4. Each material assignment has an equal probability of occurring, and the assignment is carried out by a pseudo-random process.

The procedure for determining an appropriate size of the RVE for  $FE^2$  analysis (that is, how many fixed-size elements, each with homogeneous properties, constitute a statistically representative sample of the inhomogeneous material) was determined by examining the convergence of homogenized elastic moduli as a function of RVE sizes using displacement (DISP) boundary conditions. To this end, meshes of  $4 \times 4$ ,  $10 \times 10$ ,  $20 \times 20$ ,  $40 \times 40$ , and  $80 \times 80$  elements were used and the homogenized elastic moduli values  $c_{11}$ ,  $c_{22}$ ,  $c_{44}$ , and  $c_{12}$  were computed in each case. The  $80 \times 80$  mesh was taken to generate the “exact” solution and the relative error in moduli for the remaining meshes is plotted as a function of the number of RVE elements in Fig. 10. The plot shows a clear convergence trend with an increase in RVE elements, with the  $40 \times 40$  mesh exhibiting less than a 1% difference in moduli values relative to the  $80 \times 80$  case. In addition, 10 different randomly generated realizations of the  $40 \times 40$  element mesh (each with equal particle volume fractions) were created and homogenized moduli were calculated for each one of them. Table 5 lists the mean, minimum, maximum, and standard deviation of each modulus component for the 10-RVE sample, demonstrating negligible variations in effective moduli in a  $40 \times 40$  mesh. This procedure thus demonstrates that an RVE comprising  $40 \times 40$  elements constitutes a statistically representative sample of the material microstructure and an appropriate choice for multiscale analysis. The RVE mesh used in the subsequent  $FE^2$  analysis is depicted in Fig. 11.

The mesh of the macroscopic problem in the  $FE^2$  analysis is shown in Fig. 9. It should be noted that the same RVE configuration is used to represent every RVE in the  $FE^2$  problem, which is a valid methodology given the statistically representative sample size of particles used. Given the characteristic size of the bar and the size of the particles, the fineness of the microstructure is characterized by the ratio 1:1000. In addition, given the size of the macroscopic mesh and the size of the RVE, the scale separation in the  $FE^2$  analysis is characterized by the ratio 1:12.5, which is reasonable. Given the linearity of the problem and the use of a common RVE throughout the macroscopic domain, it is



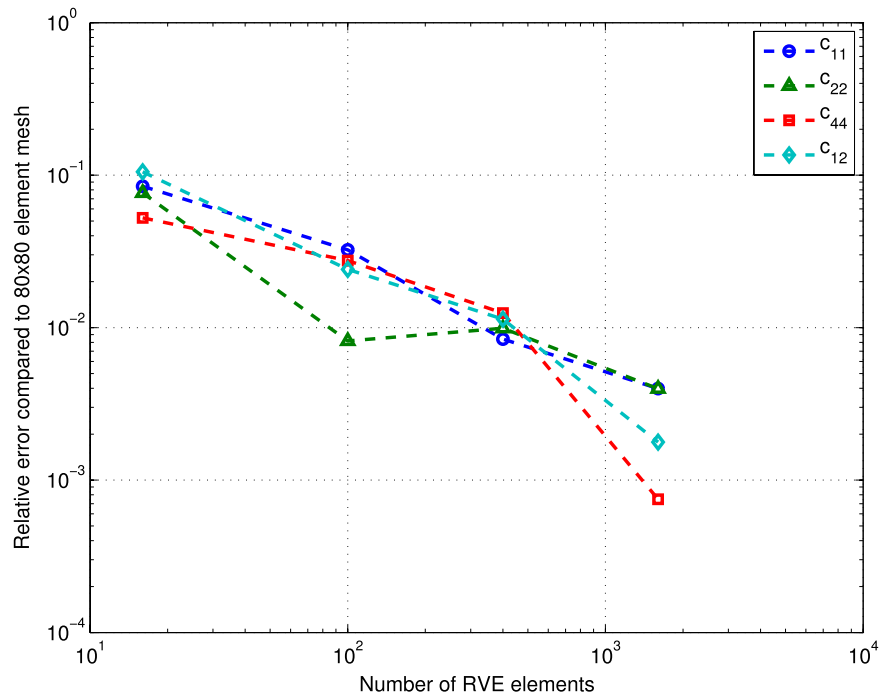


Fig. 10. Tension of a composite bar: plot of homogenized material constant values versus number of elements in RVE mesh.

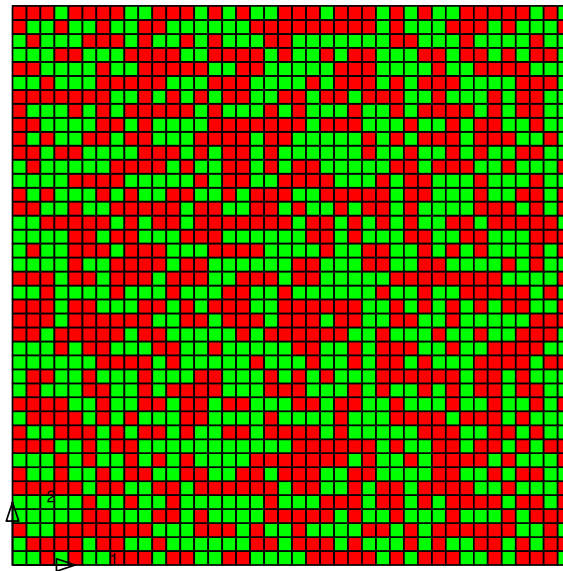


Fig. 11. Tension of a composite bar: RVE mesh (red and green elements represent particles of constituents 1 and 2, respectively). (For interpretation of the references to colour in this figure legend, the reader is referred to the web version of this article.)

possible (and, indeed, more efficient) to solve this problem in single scale upon homogenizing the material properties for a particular boundary condition choice in the RVE.

Fig. 12 compares the average horizontal displacement at the right end of the bar obtained from the single- and multi-scale analyses. The latter include both the classical Hill–Mandel (displacement and periodic) and the proposed average infinitesimal strain cases. This figure indicates that the RVE boundary conditions ECOR and ELED bracket

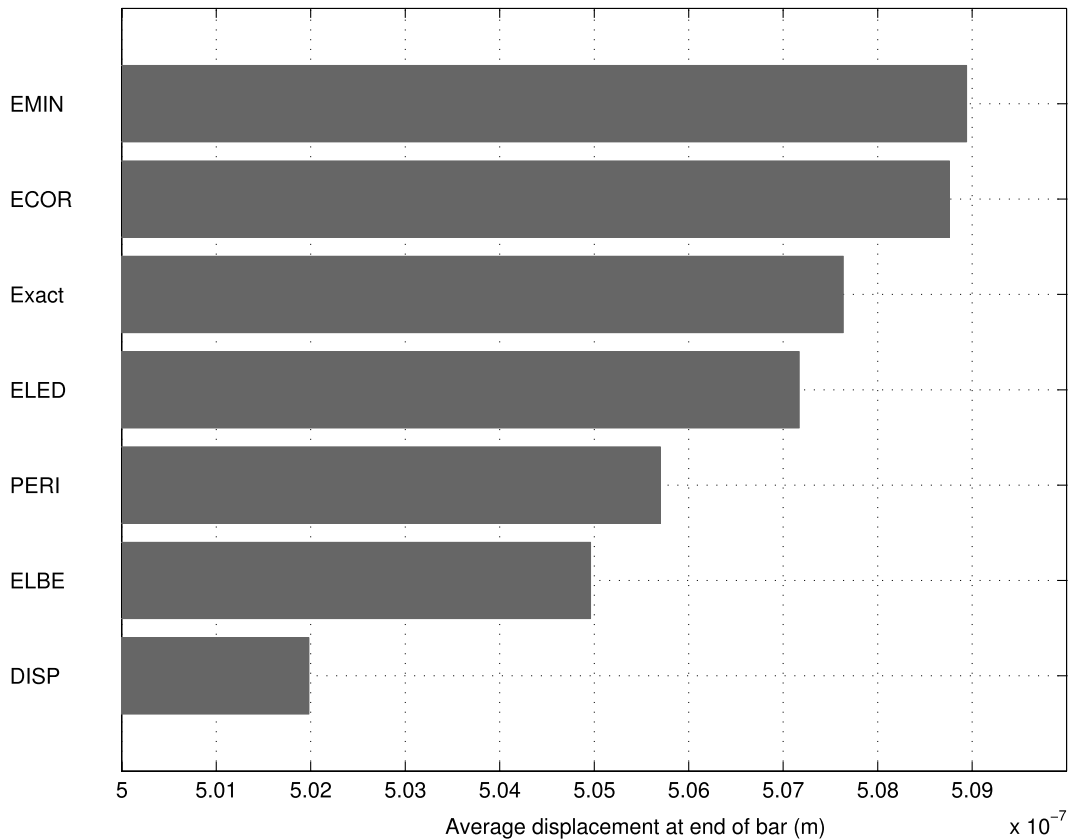


Fig. 12. Tension of a composite bar: average horizontal displacement at the right edge for single-scale analysis and multi-scale analyses using different RVE boundary conditions.

more closely the reference solution than the DISP and EMIN (effectively, traction) boundary conditions. In fact, the conditions given by ELED are able to match the reference solution to within about 0.2% error. While other solutions obtained through different RVE boundary conditions are also quite accurate for this particular problem, this observation lends further credence to the significance of the extended set of RVE boundary conditions and their ability to more closely bracket true solutions than solutions obtained through Hill–Mandel homogenization.

## 5. Conclusions

This work demonstrates conclusively that there exists a significant domain of continuum homogenization which is not constrained by the conventional Hill–Mandel condition. This greater freedom translates into a wider set of admissible boundary conditions for the RVE, which are explored in this article, as well as a natural extension to thermomechanics through a consistent calculation of homogenized flux and the inclusion of inertia by way of the fluctuations, which are deferred to later work. In the context of elasticity, it has been established here that imposing an average deformation gradient or Lagrangian strain while suppressing the translational modes (in the former) and also prescribing rotation (in the latter) through boundary conditions of the RVE yields a smooth range of homogenized material responses. These have been shown to accurately approximate the single-scale response in the case of a heterogeneous elastic bar in tension. Importantly, the results obtained from these analyses appear to span the range between the classical displacement and traction cases, while some of the boundary conditions developed in this article predict the homogenized material response with greater accuracy than standard Hill–Mandel compatible boundary conditions. The selection of boundary conditions for the RVE that yield optimally accurate solutions remains an open problem. Yet, it is important to note that such selection should be guided by the precise nature of the macroscopic problem, especially in the presence of interfaces, internal or external boundaries and other discontinuities.

## Acknowledgment

The authors would like to thank Professor Robert L. Taylor (Department of Civil and Environmental Engineering, University of California, Berkeley) for many helpful discussions on the implementation of the proposed methods and for his invaluable support on software development.

## Appendix. Consistent tangent moduli for homogenization

This appendix summarizes the calculation of the homogenized consistent tangent moduli of the RVE for the boundary-value problems discussed in Section 3.

### A.1. Tangent modulus for the $\mathbf{F}^M = \bar{\mathbf{F}}$ constraint

The homogenized referential consistent tangent modulus, expressed in component form as

$$A_{aAbB}^M = \frac{\partial P_{aA}^M}{\partial F_{bB}^M}, \quad (\text{A.1})$$

is determined with the aid of (61) by first expressing the differential  $dP_{aA}^M$  as

$$dP_{aA}^M = d\left(\frac{J^M}{v}\right) v T_{ab}^M F_{Ab}^{M-1} + \frac{J^M}{v} d\left(\int_{\omega_0} P_{aB}^m F_{bB}^m dV^m\right) F_{Ab}^{M-1} + J^M T_{ab}^M d\left(F_{Ab}^{M-1}\right). \quad (\text{A.2})$$

Subsequently, each of the differentials on the right-hand side of (A.2) are determined in terms of the differential  $dF_{bB}^M$ . Starting with the first such differential, one may use the definition of the volume  $v = \int_{\omega_0} J^m dV^m$  to write

$$\begin{aligned} d\left(\frac{J^M}{v}\right) &= \left(\frac{1}{v}\right) dJ^M - \left(\frac{J^M}{v^2}\right) dv \\ &= \left(\frac{J^M}{v} F_{Cc}^{M-1}\right) dF_{cC}^M - \frac{J^M}{v^2} \int_{\omega_0} J^m F_{Cc}^{m-1} dF_{cC}^m dV^m, \end{aligned} \quad (\text{A.3})$$

where use is made of the standard identity  $dJ = J F_{Aa}^{-1} dF_{aA}$ . Likewise, the differential in the second term of (A.2) is written with the aid of (A.1) as

$$d\left(\int_{\omega_0} P_{aB}^m F_{bB}^m dV^m\right) = \int_{\omega_0} (A_{aBcC}^m dF_{cC}^m F_{bB}^m + P_{aC}^m dF_{bC}^m) dV^m. \quad (\text{A.4})$$

Lastly, the differential  $d\left(F_{Ab}^{M-1}\right)$  in the third term of (A.2) takes the form

$$d\left(F_{Ab}^{M-1}\right) = -F_{Ac}^{M-1} F_{Cb}^{M-1} dF_{cC}^M. \quad (\text{A.5})$$

Substituting the results of Eqs. (A.3)–(A.5) into Eq. (A.2) and replacing the components of the Cauchy stress by those of the first Piola–Kirchhoff stress leads to

$$\begin{aligned} dP_{aA}^M &= P_{aA}^M \left( F_{Cc}^{M-1} dF_{cC}^M - \frac{1}{v} \int_{\omega_0} J^m F_{Cc}^{m-1} dF_{cC}^m dV^m \right) \\ &\quad + \frac{J^M}{v} \left( \int_{\omega_0} (A_{aBcC}^m dF_{cC}^m F_{bB}^m + P_{aC}^m dF_{bC}^m) dV^m \right) F_{Ab}^{M-1} - P_{aC}^M F_{Ac}^{M-1} dF_{cC}^M. \end{aligned} \quad (\text{A.6})$$

Next, the finite element interpolation (29) for the displacement in the microscale may be introduced in the components of  $d\mathbf{F}^m$ , so that (A.6) becomes

$$\begin{aligned} dP_{aA}^M &= P_{aA}^M \left( F_{Cc}^{M^{-1}} dF_{cC}^M - \frac{1}{v} \sum_{K=1}^N \left[ \int_{\omega_0} J^m F_{Cc}^{m^{-1}} \frac{\partial \phi_K}{\partial X_C} dV^m \right] d\hat{u}_c^K \right) \\ &\quad + \frac{J^M}{v} F_{Ab}^{M^{-1}} \sum_{K=1}^N \left[ \int_{\omega_0} (A_{aBcC}^m F_{bB}^m + P_{aC}^m \delta_{bc}) \frac{\partial \phi_K}{\partial X_C} dV^m \right] d\hat{u}_c^K - P_{aC}^M F_{Ac}^{M^{-1}} dF_{cC}^M. \end{aligned} \quad (\text{A.7})$$

For simplicity, the terms in (A.7) are grouped such that

$$dP_{aA}^M = \sum_{K=1}^N D_{aA,c}^K d\hat{u}_c^K + (P_{aA}^M F_{Cc}^{M^{-1}} - P_{aC}^M F_{Ac}^{M^{-1}}) dF_{cC}^M, \quad (\text{A.8})$$

where

$$D_{aA,c}^K = \frac{J^M}{v} \left[ \int_{\omega_0} (A_{aBcC}^m F_{bB}^m + P_{aC}^m \delta_{bc}) \frac{\partial \phi_K}{\partial X_C} dV^m \right] F_{Ab}^{M^{-1}} - \frac{1}{v} P_{aA}^M \left[ \int_{\omega_0} J^m F_{Cc}^{m^{-1}} \frac{\partial \phi_K}{\partial X_C} dV^m \right]. \quad (\text{A.9})$$

At this point, it is necessary to express the nodal displacement differentials  $d\hat{u}_c^K$  on the right-hand side of (A.8) in terms of the differential  $dF_{cC}^M$ . To this end, consider the system of equation (35) for the microscale problem, and assume that it has reached a converged state after a sufficient number of Newton–Raphson iterations. If the macroscopic deformation gradient is then perturbed by  $dF_{cC}^M$ , the system of equations with a converged residual may be written with the aid of (34) as

$$\begin{bmatrix} C_{ab}^{IJ} & C_{ab}^{IF} & G_{a,bB}^I \\ C_{ab}^{EJ} & C_{ab}^{EF} & G_{a,bB}^E \\ G_{cC,b}^J & G_{cC,b}^F & 0 \end{bmatrix} \begin{bmatrix} d\hat{u}_b^J \\ d\hat{u}_b^F \\ d\Lambda_{bB} \end{bmatrix} = \begin{bmatrix} 0 \\ -d\hat{f}_a^E \\ -V dF_{cC}^M \end{bmatrix}. \quad (\text{A.10})$$

In Eq. (A.10), the nodal degrees of freedom have been partitioned into free (denoted by superscripts  $I$  and  $J$ ) and fixed (denoted by superscripts  $E$  and  $F$ ). In addition,  $d\hat{f}_a^E$  represents the differential reaction forces on fixed nodal degrees of freedom due to  $dF_{cC}^M$ . Upon eliminating in (A.10) the equations associated with fixed nodal degrees of freedom, it follows that

$$\begin{bmatrix} C_{ab}^{IJ} & G_{a,bB}^I \\ G_{cC,b}^J & 0 \end{bmatrix} \begin{bmatrix} d\hat{u}_b^J \\ d\Lambda_{bB} \end{bmatrix} = \begin{bmatrix} -\sum_{F \in \text{fix}} C_{ad}^{IF} d\hat{u}_d^F \\ -V dF_{cC}^M - \sum_{F \in \text{fix}} G_{cC,d}^F d\hat{u}_d^F \end{bmatrix}. \quad (\text{A.11})$$

Recalling (24), the differential displacements for fixed nodes may be written as

$$d\hat{u}_d^F = dF_{dD}^M \hat{X}_D^F. \quad (\text{A.12})$$

Therefore, substituting this result into Eq. (A.11) the reduced system is expressed as

$$\begin{bmatrix} C_{ab}^{IJ} & G_{a,bB}^I \\ G_{cC,b}^J & 0 \end{bmatrix} \begin{bmatrix} d\hat{u}_b^J \\ d\Lambda_{bB} \end{bmatrix} = \begin{bmatrix} -\sum_{F \in \text{fix}} C_{ad}^{IF} \hat{X}_D^F \\ -V \delta_{cd} \delta_{CD} - \sum_{F \in \text{fix}} G_{cC,d}^F \hat{X}_D^F \end{bmatrix} dF_{dD}^M. \quad (\text{A.13})$$

The matrix on the left-hand side of Eq. (A.13) is identical to the stiffness matrix for the system of equations (35). If at least the minimum required boundary conditions have been applied, as discussed in Section 3.1, this matrix will be non-singular. The resulting system (A.13) is composed of nine right-hand sides, one for each of the index pairs  $(d, D)$  in  $dF_{dD}^M$ . This system yields a solution for the displacement and multiplier increments in the form

$$\begin{bmatrix} d\hat{u}_b^J \\ d\Lambda_{bB} \end{bmatrix} = \begin{bmatrix} B_{b,dD}^J \\ M_{bB,dD} \end{bmatrix} dF_{dD}^M. \quad (\text{A.14})$$

Hence, the internal displacement increments may be expressed as  $d\hat{u}_b^J = B_{b,dD}^J dF_{dD}^M$ . The Lagrange multiplier differentials are also obtained by solving the system in (A.13), but are not explicitly utilized in this macroscopic tangent computation algorithm.

Returning to Eq. (A.8) and substituting the expressions for fixed and free displacement increments from Eqs. (A.12) and (A.14), respectively, yields

$$\begin{aligned} dP_{aA}^M &= \sum_{I \in \text{free}} \left( D_{aA,c}^I B_{c,dD}^I \right) dF_{dD}^M + \sum_{E \in \text{fix}} \left( D_{aA,c}^E \hat{X}_C^E \right) dF_{cC}^M \\ &+ \left( P_{aA}^M F_{cC}^{M-1} - P_{aC}^M F_{Ac}^{M-1} \right) dF_{cC}^M. \end{aligned} \quad (\text{A.15})$$

After reindexing terms, the macroscopic tangent may be extracted from (A.15) as

$$A_{aAbB}^M = \sum_{I \in \text{free}} D_{aA,c}^I B_{c,bB}^I + \sum_{E \in \text{fix}} D_{aA,b}^E \hat{X}_B^E + \left( P_{aA}^M F_{Bb}^{M-1} - P_{aB}^M F_{Ab}^{M-1} \right), \quad (\text{A.16})$$

where  $D_{aA,n}^I$  is obtained from Eq. (A.9) and  $B_{c,bB}^I$  from Eq. (A.14).

The tangent modulus may alternatively be obtained in terms of spatial variables. In both scales, the general term of interest may be written as

$$\hat{c}_{acbd} = \frac{1}{J} F_{cA} A_{aAbB} F_{dB} = \delta_{ab} T_{cd} + c_{acbd}, \quad (\text{A.17})$$

where  $c_{acbd}$  represents the material part of the modulus, which is symmetric in the indices  $(a, c)$  and  $(b, d)$ , and is defined as

$$c_{acbd} = \frac{1}{J} F_{aA} F_{cB} \frac{\partial S_{AB}}{\partial E_{CD}} F_{bC} F_{dD}. \quad (\text{A.18})$$

Using the definitions in (A.17) and (A.18), one may push-forward the expression in Eq. (A.16) to obtain

$$\hat{c}_{acbd}^M = \frac{1}{J^M} F_{cA}^M \sum_{I \in \text{free}} \left( D_{aA,e}^I B_{e,bB}^I \right) F_{dB}^M + \frac{1}{J^M} F_{cA}^M \sum_{E \in \text{fix}} \left( D_{aA,b}^E \hat{X}_B^E \right) F_{dB}^M + \delta_{bd} T_{ac}^M - \delta_{bc} T_{ad}^M. \quad (\text{A.19})$$

Next, starting from (A.9), define  $d_{ac,e}^K$  as

$$\begin{aligned} d_{ac,e}^K &= \frac{1}{J^M} F_{cA}^M D_{aA,e}^K = \frac{1}{v} F_{cA}^M \left\{ \left[ \int_{\omega_0} \left( A_{aBeC}^m F_{bB}^m + P_{aC}^m \delta_{be} \right) \frac{\partial \phi_K}{\partial X_C} dV^m \right] F_{Ab}^{M-1} \right\} \\ &- \frac{1}{v} F_{cA}^M \left( \left[ \int_{\omega_0} J^m F_{Ce}^{M-1} \frac{\partial \phi_K}{\partial X_C} dV^m \right] T_{ab}^M F_{Ab}^{M-1} \right) \\ &= \frac{1}{v} \delta_{bc} \left[ \int_{\omega} \left( \frac{1}{J^m} F_{bB}^m A_{aBeC}^m F_{dC}^m + P_{aC}^m F_{dC}^m \delta_{be} \right) \frac{\partial \phi_K}{\partial x_d} dv^m \right] - \frac{1}{v} \delta_{bc} \left[ \int_{\omega} \frac{\partial \phi_K}{\partial x_e} dv^m \right] T_{ab}^M \\ &= \frac{1}{v} \left[ \int_{\omega} (\hat{c}_{aced}^m + \delta_{ce} T_{ad}^m) \frac{\partial \phi_K}{\partial x_d} dv^m \right] - \frac{1}{v} \left[ \int_{\omega} \frac{\partial \phi_K}{\partial x_e} dv^m \right] T_{ac}^M. \end{aligned} \quad (\text{A.20})$$

Taking into consideration the boundary condition (24) used for fixed nodes in conjunction with Eq. (A.20), the second term in (A.19) may be rewritten as

$$\frac{1}{J^M} F_{cA}^M \sum_{E \in \text{fix}} \left( D_{aA,e}^E F_{dB}^M \hat{X}_B^E \right) = \sum_{E \in \text{fix}} d_{ac,e}^E \hat{X}_d^E. \quad (\text{A.21})$$

Next, consider the product  $F_{dB}^M B_{e,bB}^I$  which appears in the first term of (A.19). Using the fixed-node boundary condition (24), the matrix equation Eq. (A.13) may be rewritten as

$$\begin{bmatrix} C_{ab}^{IJ} & G_{a,bB}^I \\ G_{cC,b}^J & 0 \end{bmatrix} \begin{bmatrix} d\hat{u}_b^J \\ d\lambda_{bB} \end{bmatrix} = \begin{bmatrix} -\sum_{F \in \text{fix}} C_{ad}^{IF} \hat{x}_e^F \\ -V\delta_{cd} F_{eC}^M - \sum_{F \in \text{fix}} G_{cC,d}^F \hat{x}_e^F \end{bmatrix} F_{De}^{M^{-1}} dF_{dD}^M. \quad (\text{A.22})$$

Eq. (A.22) yields solutions for the free displacement and Lagrange multiplier differentials, which may be expressed, as with (A.14), in the form

$$\begin{bmatrix} d\hat{u}_b^J \\ d\lambda_{bB} \end{bmatrix} = \begin{bmatrix} b_{b,de}^J \\ m_{bB,de} \end{bmatrix} F_{De}^{M^{-1}} dF_{dD}^M. \quad (\text{A.23})$$

Since the solution differentials in Eq. (A.23) must be the same as those in Eq. (A.14), it follows that

$$b_{e,bd}^J = F_{dB}^M B_{e,bB}^J. \quad (\text{A.24})$$

Using the results of Eqs. (A.20), (A.21), and (A.24), Eq. (A.19) may be simplified to

$$\hat{c}_{acbd}^M = \sum_{I \in \text{free}} d_{ac,e}^I b_{e,bd}^I + \sum_{E \in \text{fix}} d_{ac,b}^E \hat{x}_d^E + \delta_{bd} T_{ac}^M - \delta_{bc} T_{ad}^M. \quad (\text{A.25})$$

Finally, returning to Eq. (A.18) it is clear from the symmetry in the indices  $(a, c)$  and  $(b, d)$  of the material tangent modulus  $c_{acbd}^M$  that the difference  $\hat{c}_{acbd}^M - \delta_{ab} T_{cd}$  is likewise symmetric. This means that it contains at most 36 unique entries, rather than the 81 contained in the referential modulus  $A_{aAbB}^M$ . Exploiting this property allows the computation of  $b_{b,de}^J$  using only the parts symmetric in  $(d, e)$  in Eq. (A.22). This reduces the number of required solves from nine to six, which represents a significant source of computational savings, given that these must be performed for all macroscopic Gauss points in order to compute the homogenized tangent stiffness at these locations.

## A.2. Tangent modulus for the $\mathbf{E}^M = \bar{\mathbf{E}}$ constraint

The consistent tangent modulus for this boundary-value problem takes the form of (A.16) or (A.25) from Appendix A.1, where the only difference from the preceding derivation is in the calculation of the quantity  $B_{e,dD}^K$  or  $b_{e,dm}^K$ , as both of these depend directly on the boundary conditions imposed on the RVE. Therefore, this section details only the procedure used to calculate these two terms.

As in Appendix A.1, assume that a solution to the system of equation (48) has been attained after a sufficient number of Newton–Raphson iterations. Separating the nodal degrees of freedom into free and fixed and imposing a differential Lagrangian strain  $d\mathbf{E}^M$ , the system of equations for the corresponding differential displacements and Lagrange multipliers in the RVE may be written as

$$\begin{bmatrix} \tilde{C}_{ab}^{IJ} & \tilde{C}_{ab}^{IF} & \tilde{G}_{a,AB}^I \\ \tilde{C}_{ab}^{EJ} & \tilde{C}_{ab}^{EF} & \tilde{G}_{a,AB}^E \\ \tilde{G}_{cD,b}^J & \tilde{G}_{cD,b}^F & 0 \end{bmatrix} \begin{bmatrix} d\hat{u}_b^J \\ d\hat{u}_b^F \\ d\lambda_{AB} \end{bmatrix} = \begin{bmatrix} 0 \\ -d\hat{f}_a^E \\ -VdE_{CD}^M \end{bmatrix}. \quad (\text{A.26})$$

Next, the fixed displacement differentials are eliminated, resulting in the reduced system

$$\begin{bmatrix} \tilde{C}_{ab}^{IJ} & \tilde{G}_{a,AB}^I \\ \tilde{G}_{cD,b}^J & 0 \end{bmatrix} \begin{bmatrix} d\hat{u}_b^J \\ d\lambda_{AB} \end{bmatrix} = \begin{bmatrix} -\sum_{F \in \text{fix}} \tilde{C}_{ad}^{IF} d\hat{u}_d^F \\ -VdE_{CD}^M - \sum_{F \in \text{fix}} \tilde{G}_{cD,d}^F d\hat{u}_d^F \end{bmatrix}. \quad (\text{A.27})$$

Using the expression

$$dE_{CD}^M = \frac{1}{2}(F_{dC}^M \delta_{DR} + F_{dD}^M \delta_{CR}) dF_{dR}^M, \quad (\text{A.28})$$

and the relation between fixed displacement differentials and the deformation gradient differentials in (A.12), the system (A.27) becomes

$$\begin{bmatrix} \tilde{C}_{ab}^{IJ} & \tilde{G}_{a,AB}^I \\ \tilde{G}_{CD,b}^J & 0 \end{bmatrix} \begin{bmatrix} d\hat{u}_b^J \\ d\lambda_{AB} \end{bmatrix} = \begin{bmatrix} -\sum_{F \in \text{fix}} \tilde{C}_{ad}^{IF} \hat{X}_R^F \\ -\frac{1}{2} V (F_{dC}^M \delta_{DR} + F_{dD}^M \delta_{CR}) - \sum_{F \in \text{fix}} \tilde{G}_{CD,d}^F \hat{X}_R^F \end{bmatrix} dF_{dR}^M. \quad (\text{A.29})$$

The stiffness matrix in Eq. (A.29) is identical to the one for the converged state of the system of equation (48). Furthermore, if sufficient displacement boundary conditions are applied, this matrix is non-singular. Following again the procedure in Appendix A.1, the system (A.29) yields a solution of the form

$$\begin{bmatrix} d\hat{u}_b^J \\ d\lambda_{AB} \end{bmatrix} = \begin{bmatrix} \tilde{B}_{b,dR}^J \\ \tilde{M}_{AB,dR} \end{bmatrix} dF_{dR}^M. \quad (\text{A.30})$$

The quantity  $\tilde{B}_{c,bB}^I$  may then replace  $B_{c,bB}^I$  in Eq. (A.16) to obtain the tensor  $A_{aAbB}^M$  for the case of the constraint condition  $\mathbf{E}^M = \bar{\mathbf{E}}$ .

The microscale equations may also be expressed in spatial form by rewriting (A.29) as

$$\begin{bmatrix} \tilde{C}_{ab}^{IJ} & \tilde{G}_{a,AB}^I \\ \tilde{G}_{CD,b}^J & 0 \end{bmatrix} \begin{bmatrix} d\hat{u}_b^J \\ d\lambda_{AB} \end{bmatrix} = \begin{bmatrix} -\sum_{F \in \text{fix}} \tilde{C}_{ad}^{IF} \hat{X}_e^F \\ -\frac{1}{2} V (F_{dC}^M F_{eD}^M + F_{dD}^M F_{eC}^M) - \sum_{F \in \text{fix}} \tilde{G}_{d,CD}^F \hat{X}_e^F \end{bmatrix} F_{Re}^{M-1} dF_{dR}^M. \quad (\text{A.31})$$

The solution of (A.31) is now of the form

$$\begin{bmatrix} d\hat{u}_b^J \\ d\lambda_{AB} \end{bmatrix} = \begin{bmatrix} \tilde{b}_{b,de}^J \\ \tilde{m}_{AB,de} \end{bmatrix} F_{Re}^{M-1} dF_{dR}^M. \quad (\text{A.32})$$

The quantity  $\tilde{b}_{e,bd}^I$  may now be substituted for  $b_{e,bd}^I$  in Eq. (A.25) to obtain  $c_{acbd}^M$ .

### A.3. Tangent modulus for the $\mathbf{e}^M = \bar{\mathbf{e}}$ constraint

In the case of infinitesimal deformations, the material tangent modulus provides a linear relation between stresses and strains in the form

$$\sigma_{ac} = \check{c}_{acbd} \varepsilon_{bd}. \quad (\text{A.33})$$

Here, the homogenized macroscopic stress is given by

$$\boldsymbol{\sigma}^M = \frac{1}{V} \int_{\omega_0} \boldsymbol{\sigma}^m dV^m, \quad (\text{A.34})$$

which is obtained by considering Eq. (60) for infinitesimal deformations.

To obtain the homogenized modulus, combine Eqs. (A.33) and (A.34) to find that

$$\sigma_{ac}^M = \frac{1}{V} \int_{\omega_0} \sigma_{ac}^m dV^m = \frac{1}{V} \int_{\omega_0} \check{c}_{acbd}^m \varepsilon_{bd}^m dV^m = \check{c}_{acbd}^M \varepsilon_{bd}^M. \quad (\text{A.35})$$

Next, the finite element interpolation (29) for  $\hat{\mathbf{u}}$  may be invoked to write

$$\varepsilon_{bd}^m = \frac{1}{2} \left( \frac{\partial u_b^m}{\partial X_d} + \frac{\partial u_d^m}{\partial X_b} \right) = \sum_{K=1}^N \frac{1}{2} \left( \frac{\partial \phi_K}{\partial X_d} \hat{u}_b^K + \frac{\partial \phi_K}{\partial X_b} \hat{u}_d^K \right). \quad (\text{A.36})$$

Using (A.36) in conjunction with Eq. (A.35) and taking advantage of the symmetry of  $\check{c}_{acbd}^m$ , one may write

$$\check{c}_{acbd}^M \varepsilon_{bd}^M = \sum_{K=1}^N \check{d}_{ac,e}^K \hat{u}_e^K, \quad (\text{A.37})$$

where  $\check{d}_{ac,e}^K$  is given by

$$\check{d}_{ac,e}^K = \frac{1}{V} \int_{\omega_0} \check{c}_{aced}^m \frac{\partial \phi_K}{\partial X_d} dV^m. \quad (\text{A.38})$$

Eq. (A.37) may be partitioned into terms multiplying the free and fixed displacement degrees of freedom, that is,

$$\check{c}_{acbd}^M \varepsilon_{bd}^M = \sum_{I \in \text{free}} \check{d}_{ac,e}^I \hat{u}_e^I + \sum_{F \in \text{fix}} \check{d}_{ac,e}^F \hat{u}_e^F. \quad (\text{A.39})$$

In analogy to [Appendices A.1](#) and [A.2](#), the next step is to solve for the nodal displacements in terms of the macroscopic strain  $\varepsilon^M$ . Starting with Eq. (57), partitioning the nodal degrees of freedom into free and fixed, and eliminating the equations corresponding to the prescribed displacement values, the system takes the form

$$\begin{bmatrix} \check{C}_{ab}^{IJ} & \check{G}_{a,ef}^I \\ \check{G}_{ef,b}^J & 0 \end{bmatrix} \begin{bmatrix} \hat{u}_b^J \\ \mu_{ef} \end{bmatrix} = \begin{bmatrix} - \sum_{F \in \text{fix}} \check{C}_{ac}^{IF} \hat{u}_c^F \\ -V \varepsilon_{ef}^M - \sum_{F \in \text{fix}} \check{G}_{ef,c}^F \hat{u}_c^F \end{bmatrix}. \quad (\text{A.40})$$

When compared to (57), the preceding system does not include the effect of body forces. This is because the tangent modulus for linear elasticity is taken about a state of zero stress and strain, which implies that external load contributions in the microscale boundary-value problem do not enter the computation of the homogenized tangent modulus.

Since the boundary condition (51) implies that the fixed nodal displacements are related to the macroscopic strain as

$$\hat{u}_c^F = \varepsilon_{cd}^M \hat{X}_d^F, \quad (\text{A.41})$$

one may use this relation to rewrite (A.40) in the form

$$\begin{bmatrix} \check{C}_{ab}^{IJ} & \check{G}_{a,ef}^I \\ \check{G}_{ef,b}^J & 0 \end{bmatrix} \begin{bmatrix} \hat{u}_b^J \\ \mu_{ef} \end{bmatrix} = \begin{bmatrix} - \sum_{F \in \text{fix}} \check{C}_{ac}^{IF} \hat{X}_d^F \\ -V \delta_{ce} \delta_{df} - \sum_{F \in \text{fix}} \check{G}_{ef,c}^F \hat{X}_d^F \end{bmatrix} \varepsilon_{cd}^M. \quad (\text{A.42})$$

When (A.42) is solved, the resulting displacements and multipliers are expressed as

$$\begin{bmatrix} \hat{u}_b^J \\ \mu_{ef} \end{bmatrix} = \begin{bmatrix} \check{b}_{b,cd}^J \\ \check{m}_{ef,cd}^J \end{bmatrix} \varepsilon_{cd}^M. \quad (\text{A.43})$$

Substituting Eqs. (A.41) and (A.43) into (A.39) leads to

$$\check{c}_{acbd}^M \varepsilon_{bd}^M = \left( \sum_{I \in \text{free}} \check{d}_{ac,e}^I \check{b}_{e,bd}^I + \sum_{F \in \text{fix}} \check{d}_{ac,b}^F \hat{X}_d^F \right) \varepsilon_{bd}^M, \quad (\text{A.44})$$

from which it is concluded that

$$\check{c}_{acbd}^M = \sum_{I \in \text{free}} \check{d}_{ac,e}^I \check{b}_{e,bd}^I + \sum_{F \in \text{fix}} \check{d}_{ac,b}^F \hat{X}_d^F. \quad (\text{A.45})$$

Note that as with the spatial tangent in finite deformations,  $\check{c}_{acbd}^M$  is symmetric in indices  $(a, c)$  and  $(b, d)$ , hence the calculation in Eq. (A.45) is simplified by enforcing symmetry in these indices for all terms.

## References

- [1] J.M. Guedes, N. Kikuchi, Preprocessing and postprocessing for materials based on the homogenization method with adaptive finite element methods, *Comput. Methods Appl. Mech. Engrg.* 83 (1990) 143–198.
- [2] S. Ghosh, K. Lee, S. Moorthy, Multiple scale analysis of heterogeneous elastic structures using homogenization theory and voronoi cell finite element method, *Int. J. Solids Struct.* 32 (1995) 27–62.



- [3] C. Miehe, J. Schotte, J. Schröder, Computational micro–macro transitions and overall moduli in the analysis of polycrystals at large strains, *Comput. Mater. Sci.* 16 (1999) 372–382.
- [4] R.J.M. Smit, Prediction of the mechanical behavior of nonlinear heterogeneous systems by multi-level finite element modeling, *Comput. Methods Appl. Mech. Engrg.* 155 (1998) 181–192.
- [5] V.G. Kouznetsova, Computational homogenization for the multi-scale analysis of multi-phase materials (Ph.D. thesis), Eindhoven University of Technology, 2002.
- [6] C. Miehe, J. Schotte, M. Lambrecht, Homogenization of inelastic solid materials at finite strains based on incremental minimization principles. Application to the texture analysis of polycrystals, *J. Mech. Phys. Solids* 50 (2002) 2123–2167.
- [7] V.G. Kouznetsova, M.G.D. Geers, W.A.M. Brekelmans, Multi-scale constitutive modelling of heterogeneous materials with a gradient-enhanced computational homogenization scheme, *Internat. J. Numer. Methods Engrg.* 54 (2002) 1235–1260.
- [8] F. Feyel, J.-L. Chaboche,  $FE^2$  multiscale approach for modelling the elastoviscoplastic behaviour of long fiber SiC/Ti composite materials, *Comput. Methods Appl. Mech. Engrg.* 183 (2000) 309–330.
- [9] B. Nadler, P. Papadopoulos, D.J. Steigmann, Multiscale constitutive modeling and numerical simulation of fabric material, *Int. J. of Solids Struct.* 43 (2006) 206–221.
- [10] I. Özdemir, W.A.M. Brekelman, M.G.D. Geers,  $FE^2$  computational homogenization for the thermo-mechanical analysis of heterogeneous solids, *Comput. Methods Appl. Mech. Engrg.* 198 (2008) 602–613.
- [11] A. Sengupta, P. Papadopoulos, R.L. Taylor, A multiscale finite element method for modeling fully-coupled thermomechanical problems in solids, *Internat. J. Numer. Methods Engrg.* 91 (2012) 1286–1405.
- [12] R. Hill, Elastic properties of reinforced solids: Some theoretical principles, *J. Mech. Phys. Solids* 11 (1963) 357–372.
- [13] R. Hill, On constitutive macro-variables for heterogeneous solids at finite strain, *Proc. R. Soc. Lond. Ser. A* 326 (1972) 131–147.
- [14] M.G.D. Geers, V.G. Kouznetsova, W.A.M. Brekelmans, Multi-scale computational homogenization: Trends and challenges, *J. Comput. Appl. Math.* 234 (2010) 2175–2182.
- [15] C. Miehe, A. Koch, Computational micro-to-macro transitions of discretized microstructures undergoing small strains, *Arch. Appl. Mech.* 72 (2002) 300–317.
- [16] K.K. Mandadapu, A. Sengupta, P. Papadopoulos, A homogenization method for thermomechanical continua using extensive physical quantities, *Proc. R. Soc. A* 468 (2012) 1696–1715.
- [17] J.H. Irving, J.G. Kirkwood, The statistical mechanical theory of transport processes. IV. The equations of hydrodynamics, *J. Chem. Phys.* 18 (1950) 817–829.
- [18] J. Fish, R. Fan, Mathematical homogenization for nonperiodic heterogeneous media subjected to large deformation transient loading, *Internat. J. Numer. Methods Engrg.* 76 (2008) 1044–1064.
- [19] C. Truesdell, W. Noll, The non-linear field theories of mechanics, in: S. Flügge (Ed.), *Handbuch Der Physik III/3*, Springer-Verlag, Berlin, 1965.
- [20] R.L. Taylor, FEAP—A Finite Element Analysis Program, User Manual: v8.4. University of California, Berkeley. <http://www.ce.berkeley.edu/feap>.
- [21] R.L. Taylor, FEAP—A Finite Element Analysis Program, Programmer Manual: v8.4. University of California, Berkeley. <http://www.ce.berkeley.edu/feap>.
- [22] R.L. Taylor, FEAP—A Finite Element Analysis Program,  $FE^2$  Manual: v8.4. University of California, Berkeley. <http://www.ce.berkeley.edu/feap>.
- [23] Open MPI: Open source high performance computing. <http://open-mpi.org>.